Impact of offshore and onshore wind profiles on ground generation airborne wind energy system performance

Markus Sommerfeld[1], Martin Dörenkämper[2], Jochem De Schutter[3], and Curran Crawford[1]

[1]Institute for Integrated Energy Systems, University of Victoria, British Columbia, Canada
[2]Fraunhofer Institute for Wind Energy Systems (IWES), Oldenburg, Germany
[3]Systems Control and Optimization Laboratory IMTEK, University of Freiburg, Germany

Correspondence: Markus Sommerfeld (msommerf@uvic.ca)

Abstract. Airborne wind energy systems (AWESs) aim to operate at altitudes above conventional wind turbines (WTs) and harvest energy from stronger winds aloft. This study investigates these claims by determining dynamic, power-optimal flight trajectories, operating heights subject to realistic offshore and onshore wind conditions. The utilized wind speed profiles are based on simulated offshore and onshore 10-minute mesoscale wind conditions which are analyzed and categorized using k-means clustering. To reduce computational cost of the trajectory optimization, representative wind speed profiles from each cluster are implemented into the awebox optimal control model to determine feasible, power-optimal trajectories. The results describe the influence of wind speed magnitude and profile shape on optimal trajectories, tether speed, tether length and tension. Optimal operating heights are generally below 400 m with most AWES operating at around 200 m. This study compares power curve visualizations for a constant reference height of 100 m to an apriori operating altitude guess of 100 - 400 m to the pattern trajectory height. Power curves are estimated based on average cycle power and compared to wind turbine (WT) and quasi-steady-state AWES reference model (QSM) performance. A power curve comparison between mesoscale-simulated wind conditions and logarithmic wind speed profiles shows that the offshore location is reasonably well approximated by logarithmic wind speed profiles. Realistic wind data onshore often outperform the logarithmic reference due to the higher number of non-monotonic wind speed profiles.

1 Introduction

Airborne wind energy systems (AWESs) aspire to harvest stronger and less turbulent winds at mid-altitude, here defined as heights above 100 m and below 1000 m, presumably beyond what is achievable with conventional wind turbines (WTs). The prospects of higher energy yield combined with reduced capital cost motivate the development of this novel class of renewable energy technology (Lunney et al., 2017; Fagiano and Milanese, 2012). Unlike conventional WTs, which over the last decades have converged to a single concept with three blades and a conical tower, several different concepts and designs are still under investigation by numerous companies and research institutes (Cherubini et al., 2015). These kite-inspired systems consist of three main components: one or more flying wings or kites, one or more ground stations and one or more tethers to connect them. This study focuses on the two-phase, ground generation concept, also referred to as pumping mode. During the reel-out phase the wing pulls a tether from a drum on the ground which is connected to a generator, thereby producing electricity. This

is followed by the reel-in phase during which the kite adjusts its angle of attack to reduce the aerodynamic forces and return to its initial position. Various other concepts such as fly-gen, aerostat or rotary lift are not considered in this study (Cherubini et al., 2015).

Since this technology is still at a relatively early stage of development, validation and comparison of results is difficult. A standardized power curve definition and reference design, similar to Jonkman et al. (2009) or Gaertner et al. (2020), will enable comparison between different concepts and to conventional wind turbines. It is not the goal of this study to determine such a general power curve, but rather investigate the variation in power stemming from realistic wind profiles of a specific type of machine. Recent consensus among the community defined a power curve as the maximum average cycle power as a function of the wind speed at pattern height, which is the time-averaged height during the reel-out power-producing phase (Airborne Wind Europe, 2021). Together with the site-specific wind resource, power curves can be used by wind park planners and manufacturers to estimate the annual energy production (AEP), levelized cost of electricity (LCOE) and determine financial viability (Malz et al., 2020a). The glossary does not define an estimation method for these metrics. In contrast to conventional WTs, where the wind speed probability distribution at hub height is used to determine AEP, AWES continuously change their operating height, making it difficult to determine the AEP with this approach. Furthermore, the performance of AWESs is highly dependent on the shape and magnitude of the wind speed profile over a range height from which the wind energy is harvested. Simple wind profile approximations using logarithmic or exponential wind speed profiles, which are often erroneously applied beyond earth's surface layer (Optis et al., 2016), might approximate long-term average conditions, but cannot capture the broad variation of profile shapes that exist on short timescales (Emeis, 2013). They are therefore an inappropriate approximation of instantaneous wind conditions and do neither capture diurnal nor seasonal changes, which decreases the quality of the predicted power output. However, they can be employed to estimate average performance and are the standard in most AWES power estimation studies. Heilmann and Houle (2013) used exponential wind speed profiles with a wind shear exponent of 0.15 and a standard Rayleigh distribution with 7 ms^{-1} to estimate performance and cost. nneberg et al. (2018) describes the performance of a soft kite pumping mode AWES with a family of power curves at different fixed altitudes, which correspond to the findings in this research. Leuthold et al. (2018) investigated power-optimal trajectories and performance of a ground generation multi kite configuration for a range of logarithmic wind speed profiles. Licitra et al. (2019) estimated the performance and power curve of a ground generation, fixed-wing AWES by generating power-optimal trajectories and validating them against Ampyx Power AP2 data (Licitra, 2018; Malz et al., 2019; Ampyx, 2020), which is also used in this research. The optimal, single-loop trajectory was defined by a simple power law approximation of the wind speed profile. Because of the upscaling drawbacks of single-kite AWES, De Schutter et al. (2019) analyzed the performance of utility scale, stacked multi-kite systems, using the same optimization framework as the present research. Onshore and offshore logarithmic wind speed profiles served as boundary conditions for the non-linear optimization problem. Malz et al. (2020b) maximized performance, based on the model described in Malz et al. (2019), similar to the present research, to reduce the overall computation times, wind data were clustered into characteristic profile shapes and sorted by average wind speed. This allowed for the initial guesses of every subsequent optimization to be based on the previous results. Aull et al. (2020) explored the design and sizing of fly-gen rigid-wing systems based on a steady-state model with simple aerodynamic and mass-scaling approximations. The wind resource was described by an exponential wind shear

model with Weibull distribution. Bechtle et al. (2019) used ERA5 data to assess the wind resource at higher altitudes for entire Europe. The authors describe the available wind energy without accounting for a specific conversion mechanism. The investigation includes a description of wind speed and probability for several heights. Schelbergen et al. (2020) compared the energy production computed from this data set to the production computed from the Dutch Offshore Wind Atlas (DOWA) and light detection and ranging (LiDAR) data. Principal component analysis and k-means clustering was used to determine representative wind speed profiles for a part of the Netherlands and the North Sea. They derived power curves and estimated AEP from wind statistics for several locations. Faggiani and Schmehl (2018) investigated aspects of joint operation, such as spacial stacking of the systems and phase-shifted operation of several 100 kW soft wing pumping kite systems arranged in a wind park. Performance was estimated using a quasi-steady-state model (QSM) (Schmehl et al., 2013; van der Vlugt et al., 2019), similar to the one used in the present research, subject to a standard logarithmic wind profile.

Wind profiles are governed by weather phenomena, environmental and location-dependent conditions (e.g. surface roughness) on a multitude of temporal and spatial scales. The preferred means of determining wind conditions for wind energy converters are long-term, high resolution measurements, which at mid-altitudes can solely be achieved by long-range remote sensing such as LiDAR or SoDAR (sonic detection and ranging). Measuring wind conditions at mid-altitudes is costly and difficult, due to reduced data availability (Sommerfeld et al., 2019a). Additionally, publicly available measurements are scarce. Therefore, we decided to base this study on wind data derived from Weather Research and Forecasting model (WRF) mesoscale simulations (Skamarock et al., 2008). However, the described trajectory optimization methodology can be applied to any wind data set such as wind atlas data or measurements. Numerical mesoscale weather prediction models such as the WRF, which is well known for conventional WT siting applications (Salvação and Guedes Soares, 2018; Dörenkämper et al., 2020), are used to estimate wind conditions on time scales of a few minutes to years. Sommerfeld et al. (2019b) compares the simulated onshore data used in this study, located in northern Germany near the city of Pritzwalk, to LiDAR measurements and found a good, but altitude-dependent agreement between both data sets . The simulated offshore conditions used in this study can be references against data at the FINO3 research platform in the North Sea. This study investigates AWES performance subject to 10-minute average wind data, which is the standard for conventional WT, while the New European Wind Atlas (NEWA) only provides 30-minute average data (Witha et al., 2019). We use this higher resolution wind data because the higher temporal, spatial and vertical resolution reduces averaging and allows for the investigation of more realistic wind conditions.

The key contribution of this paper is the investigation of power-optimal AWES performance subject to realistic onshore and offshore wind profiles and its impact on average cycle power variation. Therefore, WRF-simulated wind data are used instead of assuming a wind profile relationship such as the logarithmic or exponential wind profile. Furthermore, this study is a continuation of previous analyses of LiDAR measurements (Sommerfeld et al., 2019a) and WRF simulations (Sommerfeld et al., 2019b) at the onshore location. To justify the realism of the data location specific characteristics are described. The data are categorized using k-means clustering which classifies the wind data at each location into groups of similar wind speed magnitude and vertical profile shape. From these clusters three representative profiles are sampled and implemented into the awebox optimization toolbox as boundary conditions. By selecting these profiles based on their average wind speed between 100 and

400 m, which is an apriori guess of the pattern trajectory height (Airborne Wind Europe, 2021), we use actual simulated data instead of averaged data. By choosing the 5th, 50th, 95th percentiles, we encompass the most likely operating conditions within each cluster and avoid non-representative profile extrema. This drastically reduces the computational cost as only few selected profiles are needed to represent the entire wind spectrum. This study only uses 60 out of 52560 10-minute wind speed profiles. This is sufficient for the scope of this study, which includes the analysis of representative operating conditions and the estimation of power curves.

The `awebox` optimization model allows for the investigation of dynamic performance parameters, such as aircraft trajectories, tether tension, tether speed and power which highly depend on the wind conditions. The aircraft model is based on the well investigated and published Ampyx Power AP2 prototype (Licitra, 2018; Malz et al., 2019; Ampyx, 2020), scaled to a wing area of $A = 20 \text{ m}^2$. The optimized average cycle powers are referenced against optimal performance subject to a simple logarithmic wind speed profile, a quasi-steady-state reference AWES model, and a steady-state WT power estimation. The apriori guess of 100 and 400 meter reference height is verified by comparing AWESs power curves over wind speed at reference height to wind speed at pattern trajectory height.

The paper is structured as follows: Section 2 introduces the mesoscale WRF model setup, first Section 2.2 analyzing the onshore and offshore wind resource, then Section 2.3 introducing the k-means clustering algorithm and summarizing the results of clustered wind profiles (both longitudinal and lateral wind components). For visualization purposes data are shown for $k = 10$ clusters, while 20 clusters are used in the later analysis. Section 3 introduces the dynamic AWES model, comprising of aircraft, tether and ground-station models. Section 4 describes the `awebox` optimization framework, summarizes the aircraft parameters, system constraints and initial conditions. This is followed by a description of the wind, WT and AWES reference models in Section 5. Section 6 presents the results which include flight trajectories and time series of various performance parameters, a statistical analysis of tether length and operating altitude as well as a power curve estimation. Finally, Section 7 concludes with an outlook and motivation for future work.
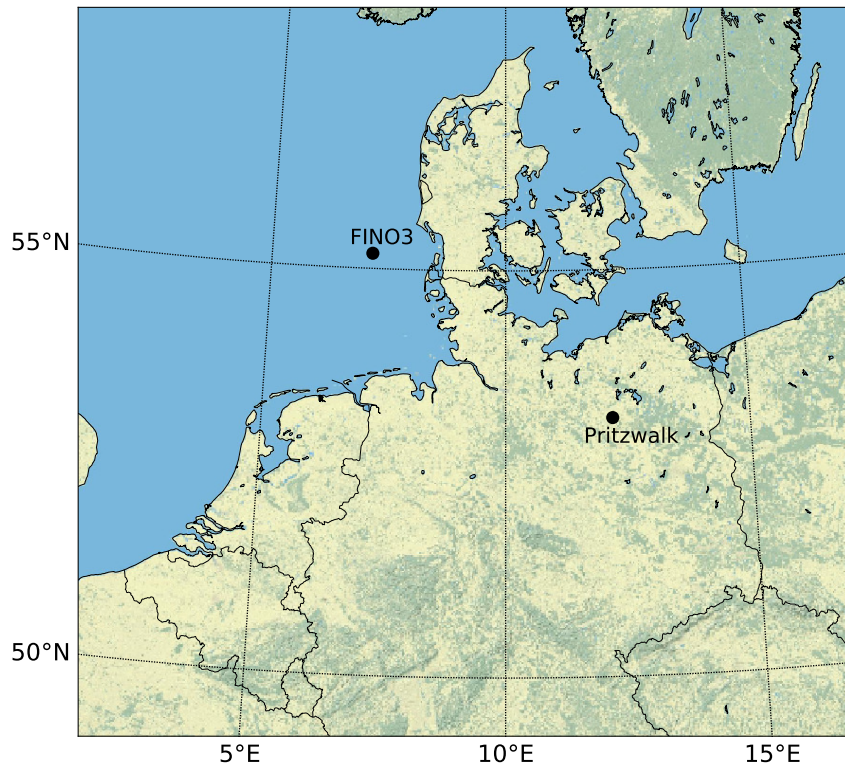
2 Wind conditions

As of now, no universally accepted mid-altitude AWES reference wind model exists. Therefore, we analyze onshore and offshore wind conditions based on the mesoscale WRF model introduced at two locations in a Sub-section 2.1. Sub-section 2.2 analyses wind statistics to give an insight into the wind regime at both locations. Clustering, introduced in Sub-section 2.3, is used to determine groups of similar vertical wind profiles from which unaveraged, representative profiles are sampled. This significantly reduces the computational cost as only few selected profiles are necessary to represent the wind regime and to approximate the power curves. Sub-sections 2.4 and 2.5 describe the resulting clusters and their statistical correlation with temporal and meteorological phenomenon.

2.1 Mesoscale simulations

This study compares AWES performance for onshore and offshore locations in Europe (Figure 1). Wind conditions for the chosen years are assumed to be representative of these locations. However, the wind data has not been compared to long-term wind atlas data and has not been corrected using long-term simulations. The onshore data represents wind conditions at the Pritzwalk Sommersberg airport (lat: $53°10'47.00''$N, long: $12°11'20.98''$E) in northern Germany and comprises 12 months of WRF simulation data between September 2015 and September 2016. The area surrounding the airport mostly consists of flat agricultural land with the town of Pritzwalk to the south and is therefore a fitting location for wind energy generation (Sommerfeld et al., 2019a, b). The FINO3 research platform in the North Sea (lat: $55°11,7'$N, long: $7°9,5'$ E) was chosen as a representative offshore location due to the proximity to several offshore wind farms and the amount of comprehensive reference measurements (Peña et al., 2015). The offshore simulation covers the time frame between September 2013 and September 2014.

The mesoscale simulations used the Weather Research and Forecasting (WRF) model. The onshore simulation was performed with version 3.6.1 (Skamarock et al., 2008) prior to the 2018 release of WRF version 4.0.2 (Skamarock et al., 2021) in which the offshore simulations were computed. The setup of the model was adapted and constantly optimized for wind energy applications by the authors of the present manuscript in the framework of various projects and applications in recent years (Dörenkämper et al., 2015, 2017; Dörenkämper et al., 2020; Hahmann et al., 2020; Sommerfeld et al., 2019b). The focus of this study is not on the detailed comparison between mesoscale models, but on AWES performance subject to realistic onshore and offshore wind conditions. Both WRF models provide adequate wind data for performance assessment, even though the setup and time frame are different.

Each simulation consists of three nested domains around their respective location (black dot) shown in Figure 1. Atmospheric boundary conditions are defined by ERA-Interim (Dee et al., 2011) for the onshore location and by ERA5 (Hersbach and Dick, 2016) reanalysis data for the offshore location, while sea surface parameters for the offshore location are based on OSTIA (Donlon et al., 2012). These data sets have proven to provide good results for wind energy relevant heights and sites (Olauson, 2018; Hahmann et al., 2020). Both simulations use the MYNN 2.5 level scheme for the planetary boundary layer (PBL) physics (Nakanishi and Niino, 2009). While the onshore simulation was performed in a single 12 month spanning simulation (2015-09-01 to 2016-08-31), the offshore simulation period consisted of 410 days (2013-08-30 to 2014-10-14) that was split into 41 simulations of 10 days each with an additional 24 hours of spin-up time per run. Spin-up describes the period during which the model produces unreliable results due to the initialization based on a coarser, global atmospheric reanalysis data set. The data at every vertical, terrain-following, pressure coordinate (sigma level) are transformed to the geometric heights using the post-processing methodology described in Dörenkämper et al. (2020). Table 1 summarizes the key parameters of the model settings used in this study. All simulations were run on the *EDDY* High-Performance Computing clusters at the University of Oldenburg (Carl von Ossietzky Universität Oldenburg, 2018).

Figure 1. Map of northern Germany with the representative onshore (Pritzwalk) and offshore (FINO3) locations highlighted by black dots.

2.2 Wind regime

Figure 2 depicts the wind roses of the computed annual wind conditions at 100 m (a,b) and 500 m (c,d) height onshore (left) and offshore (right). The dominant wind direction at both locations is southwest, turning clockwise with increasing altitude.

160   Directional variability decreases and wind speed increases with height, following the expected trends in the northern hemisphere (Arya and Holton, 2001; Stull, 1988). The average onshore wind direction turns about $14°$ between 100 and 500 m, whereas average offshore wind direction only veers approximately $5°$. The offshore wind direction turns approximately $10°$ additional degrees above 500 m, resulting in roughly the same westerly wind direction at ~~high altitudes at~~ around 1000 m. Due to the prevailing unstable conditions offshore, ~~which are~~ accompanied by strong vertical mixing, the investigated heights show

165 less veer than onshore. The wind shear at the offshore location is lower compared to the onshore location due to lower surface roughness.

Table 1. Key setup parameters of the onshore and offshore mesoscale WRF simulations (Skamarock et al. 2008)

Model Parameter	Settings	
	Onshore	Offshore
WRF model version	3.5.1	4.0.2
Time period	2015-09-01 to 2016-08-31	2013-08-30 to 2014-10-14
Reanalysis data set	ERA-Interim	ERA5 & OSTIA
Horizontal grid size (D01, D02, D03)	120×120, 121×121, 121×121	150×150, 151×151, 151×151
Horizontal Resolution (D01, D02, D03)	27 km, 9 km, 3 km	18 km, 6 km, 2 km
Vertical levels grid	60 sigma levels (about 25 below 2 km)	60 sigma levels (about 25 below 2 km)
Nesting	1-way	1-way
Initialisation strategy	single run	240 h runs plus 24 h spinup time
Nudging	Analysis nudging (FDDA)	Analysis nudging (FDDA)
PBL scheme	MYNN level 2.5 scheme	MYNN level 2.5 scheme
Micro physics	Ferrier scheme	WRF Single–moment 5–class scheme
Long wave & shortwave radiation	RRTM & Dudhia	RRTMG scheme

Figure 3 shows the annual horizontal wind speed probability distributions at each height level for both locations. These distributions give an insight into the wind speed statistics at specific heights, but not into the statistics of the wind profile shapes. The chosen nonlinear color gradient allows for the representation of the entire relative probability range. Onshore (a) wind speeds are relatively low and have a fairly narrow deviation below 300 m, due to dominant surface effects. Above this height the distribution broadens, but a high probability of low wind speeds remains for the full height range. The distributions show bimodal characteristics caused by different atmospheric stratification. Low wind speeds are commonly associated with unstable and high wind speeds with neutral or stable atmospheric conditions.

Such multimodal distributions at higher altitudes are better described by the sum of two or more probability distributions, as standard Weibull or Rayleigh distributions cannot capture this phenomenon (Sommerfeld et al., 2019a). Offshore (b) wind speeds display a wider distribution at all heights as they are less affected by surface effects. Similar to onshore, the offshore frequency distribution also shows a high probability of lower wind speeds (between 5-10 ms^{-1}) at all heights. Higher wind speeds at lower altitudes benefits conventional WT and weakens the argument for offshore AWES as one of their benefits would be to harness energy from the stronger winds at higher altitudes. Additional reasons for placing AWES offshore are safety and land use regulations and potential cost benefits of a smaller support structure (offshorewind.biz, 2018; Lunney et al., 2017; Ellis and Ferraro, 2016).

Atmospheric stability of the boundary layer, which highly affects the wind speed profile shape, is commonly characterized using the Obukhov length $\mathcal{L}$ (Obukhov, 1971; Sempreviva and Gryning, 1996). Here, the concept is extended to mid-altitudes. $\mathcal{L}$ is defined by the simulated friction velocity u_*, virtual potential temperature θ_v, potential temperature θ, kinematic
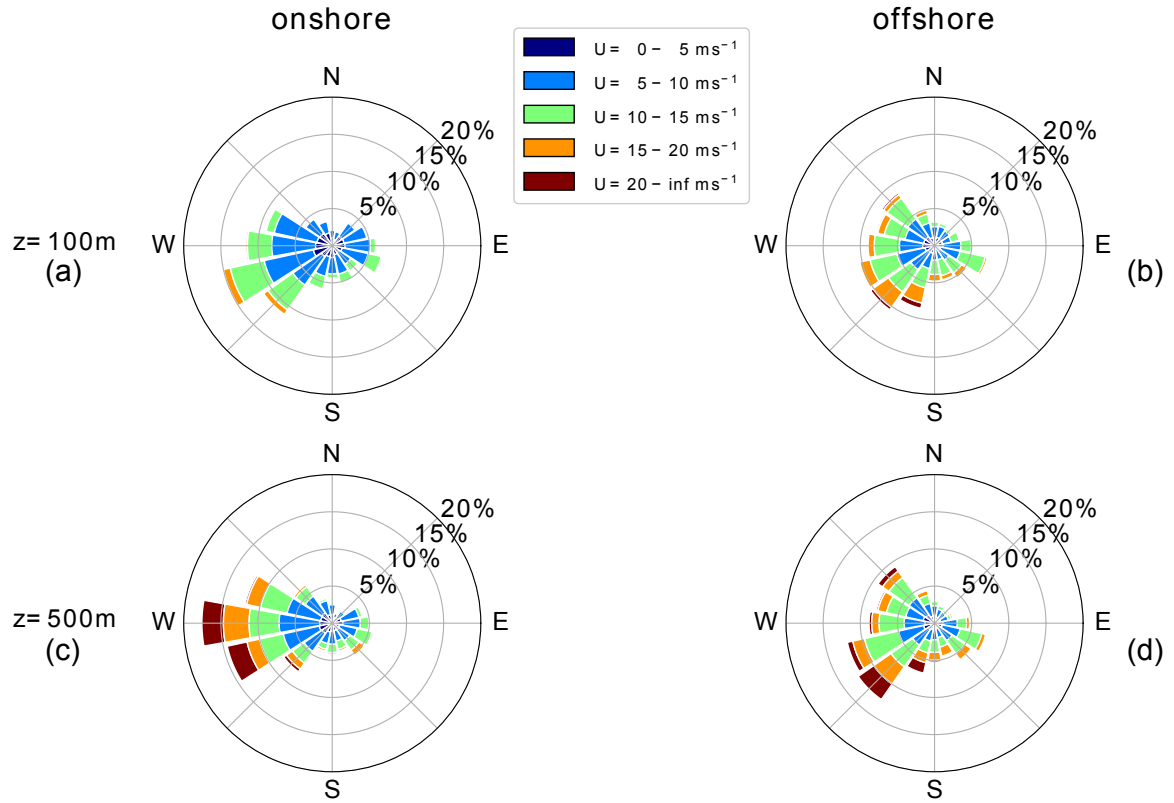
Figure 2. Wind roses of annual wind direction and speed statistics at Pritzwalk (onshore) and FINO3 (offshore) for 100 and 500 m during the simulated year.

virtual sensible surface heat flux Q_S, kinematic virtual latent heat flux Q_L, the von Kármán constant k and gravitational acceleration g:

$$\mathcal{L} = \left(\frac{-u_*^3 \theta_\mathrm{v}}{kg}\right)\left(\frac{1}{Q_\mathrm{S}} + \frac{0.61}{Q_\mathrm{L}\theta}\right). \tag{1}$$

Various stability classifications using the Obukhov length are defined for different wind energy sites. Table 2 summarizes the Obukhov length bin widths (Floors et al., 2011) and the frequency of occurrence of each stability class onshore and offshore, consistent with Sommerfeld et al. (2019b).

Neutral stratification occurs approximately 20% of the year at both locations. The lower heat capacity of the land surface leads to a faster heat transfer and a quicker surface cool-off which favors the development of stable stratification ($\approx$17% onshore vs $\approx$6% offshore). The offshore location has a higher probability of unstable conditions which is likely caused by a warmer ocean surface compared to the air above (Archer et al., 2016).
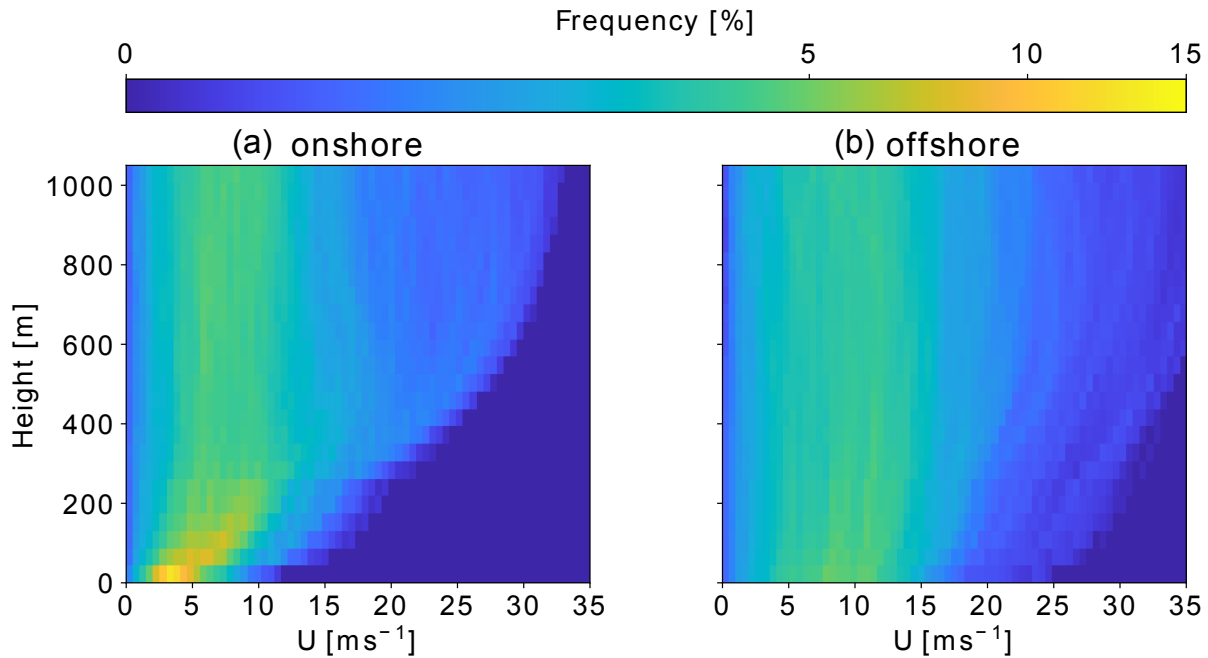
Figure 3. Comparison of WRF-simulated annual wind speed probability distribution at each height level between Pritzwalk (onshore left) and FINO3 (offshore right) up to 1000 m. A nonlinear color scheme is chosen to represent the high probability of low altitude onshore winds while still differentiating the lower, wide spread frequencies at higher altitudes.

Table 2. Stability classes based on Obukhov lengths (Floors et al., 2011) and associated annual probability at Pritzwalk ~~(onshore: 01.09.2015 – 31.08.2016)~~ and FINO3 ~~(offshore: 30.08.2013 – 14.10.2014)~~, based on WRF results.

Stability class	$\mathcal{L}$ [m]	onshore	offshore
Unstable (U)	$-200 \leq \mathcal{L} \leq -100$	7.27%	13.66%
Nearly unstable (NU)	$-500 \leq \mathcal{L} \leq -200$	7.09%	16.34%
Neutral (N)	$|\mathcal{L}| \geq 500$	20.71%	22.82%
Nearly stable (NS)	$200 \leq \mathcal{L} \leq 500$	12.56%	5.15%
Stable (S)	$50 \leq \mathcal{L} \leq 200$	17.24%	6.20%
Very stable (VS)	$10 \leq \mathcal{L} \leq 50$	10.04%	2.96%
Other	$-100 \leq \mathcal{L} \leq 10$	25.09%	32.87%

195   Both unstable and stable conditions can lead to non-logarithmic and non-monotonic wind speed profiles. Unstable conditions are often accompanied by almost uniform wind speed profiles due to increased mixing, whereas low-level jets (LLJs) can develop during the nocturnal stable onshore boundary layer (Banta, 2008). Both locations have a high chance of unassigned

9

conditions (labeled as "Other") which are mostly associated with low wind speeds. All of which affect AWES operation conditions and power production.

2.3 Clustering of wind conditions

An accepted methodology to describe the near-surface atmosphere is atmospheric stability, commonly quantified by the Obukhov length (Obukhov, 1971; Sempreviva and Gryning, 1996) which exclusively uses surface data (Section 2.2 and Equation (1)). Previous studies (Sommerfeld et al., 2019a, b) showed that Obukhov-length-classified wind speed profiles diverge with height, especially during neutral and stable conditions, which indicates vertically heterogeneous atmospheric stability and suggests that surface-based stability categorization is insufficient for higher altitudes. Clustering wind velocity profiles based on their similarity results in more cohesive profile groups (Schelbergen et al., 2020). In contrast to classifying the wind regime by atmospheric stability, which requires additional temperature and heat flux data, clustering only uses wind data at multiple heights and groups profiles by similarity. Therefore, clustering can also be applied to wind-only measurements such as LiDAR.

The k-means clustering algorithm (Pedregosa et al., 2011) used in this study is chosen for its ease of use and scalability, due to the high dimensionality of the data set. Many other algorithms produce similar results, but a comparison between clustering algorithms is beyond the scope of this research. Before clustering, the two horizontal wind velocity components u and v, whose vertical variation define the wind velocity profile, are rotated such that the main wind component (average wind direction between 100 m and 400 m) u_{main} points in the positive x direction and the transverse component u_{dev} is perpendicular to it, pointing in the positive y direction. This removes the directional dependency of the wind velocity profiles, results in more homogeneous clusters and simplifies the comparison of wind data and `awebox` results. It is analogous to assuming omnidirectional operation. The trajectory optimization still needs to adjust to changes in wind conditions with height.

The wind velocity data set up to 1000 m comprises of data points at 30 height levels and in 2 directions. The clustering algorithm assigns each data point to one of k clusters represented by their respective cluster mean, also called "centroid". These centroids are chosen such that they minimize the sum of the Euclidean distances to every data point within each cluster. This cost function is also referred to as "inertia" or "within-cluster sum-of-squares". As such, the centroids are usually not actual data points, but rather the clusters' average, and will at best coincide with a data point by chance. The resulting cluster label is the result of random initialization and does not have any mathematical meaning. We therefore sort and label the clusters by average wind speed between 100 m - 400 m for the following analyses in Sub-section 2.4. The variable k refers to the fixed, predefined number of clusters. The choice of k significantly affects the accuracy of the wind resource description as well as the computational cost. The choice of k is informed by the elbow method, named after the characteristic line chart which resembles an arm, and silhouette score. The "elbow" (the point of inflection on the curve) is a good indication that the underlying model fits well for the corresponding number of clusters. k can be chosen at a point where the inertia reduction becomes marginally small or decreases linearly (Pedregosa et al., 2011). Absolute values of inertia are not a normalized metric and therefore scales with size of the considered data set. The silhouette coefficients on the other hand are normalized between -1 (worst) and 1 (best). They indicate the membership of a data point to its cluster in comparison to other clusters, i.e. proximity of each data point in one cluster to data points in neighboring clusters (Pedregosa et al., 2011). A negative value suggests that a data point

is assigned to the wrong cluster. The silhouette score is the average of all silhouette coefficients for a fixed number of clusters k.

Figure 4 (a) shows the inertia (within-cluster sum-of-squares) for both locations. Figures 4 (b) and 4 (d) show the silhouette coefficients for every cluster for $k = 10$, which is chosen here for visualization purposes. The corresponding average silhouette score is depicted by a dashed, red, vertical line. Each cluster is sorted by average wind speed between 100 ~~m~~ and 400 m and color coded corresponding to centroid average wind speed, same as Figure 5. Performing this silhouette score analysis for multiple k results in the trend shown in Figure 4 (c). A k ~~of~~ 20 seems to be a decent choice for the available data sets as inertia only decreases moderately for higher number of clusters which does not justify the additional computational cost. Similarly, the silhouette score remains almost constant for higher numbers of clusters. Therefore, $k = 20$ has been chosen for later analyses in Section 6.
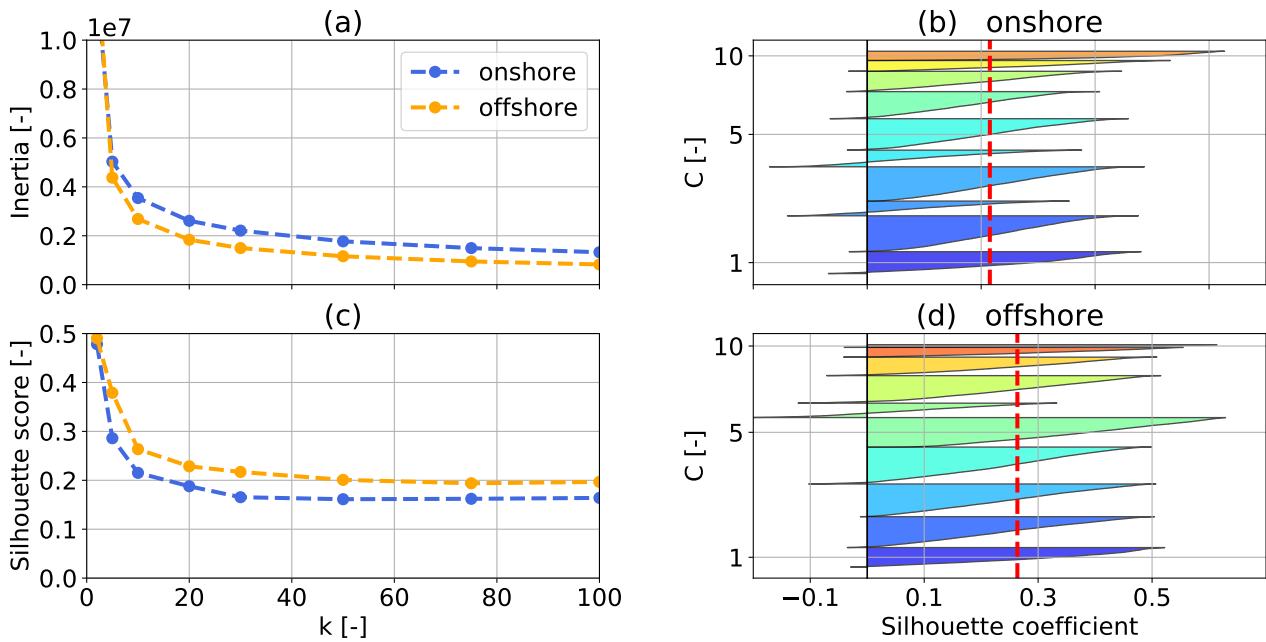

Figure 4. k-means clustering inertia over of number of clusters k (a) for one year of onshore (blue) and offshore (orange) wind velocity profiles up to 1000 m. The Onshore (b) and offshore (d) silhouette coefficients express the distance to neighbouring clusters and are color coded according to average wind speed between 100 and 400 m, same as in Figures 5 7, 8 and 9. The red dashed line represents the silhouette score, which is the average silhouette coefficient. Silhouette score (c) over number number of cluster k for both locations. The number of clusters $k = 10$ has been chosen for presentation purposes only. Later analyses use $k = 20$ clusters.

2.4 Analysis of clustered profiles

For visualization purposes, the following Sub-sections describe the wind conditions at both locations using only $k = 10$ clusters. Later analyses use $k = 20$ clusters.

245   Figures 5 (a) and 5 (b) show the average ~~profiles~~ of the clustered wind ~~velocity~~ profiles, also referred to as centroids. Their color corresponds to the average wind speed between 100 and 400 m. All WRF-simulated wind speed profiles are depicted in gray. Clusters are sorted by average centroid speed between 100 and 400 m, represented by their colors and labels ($C = 1 - 10$).
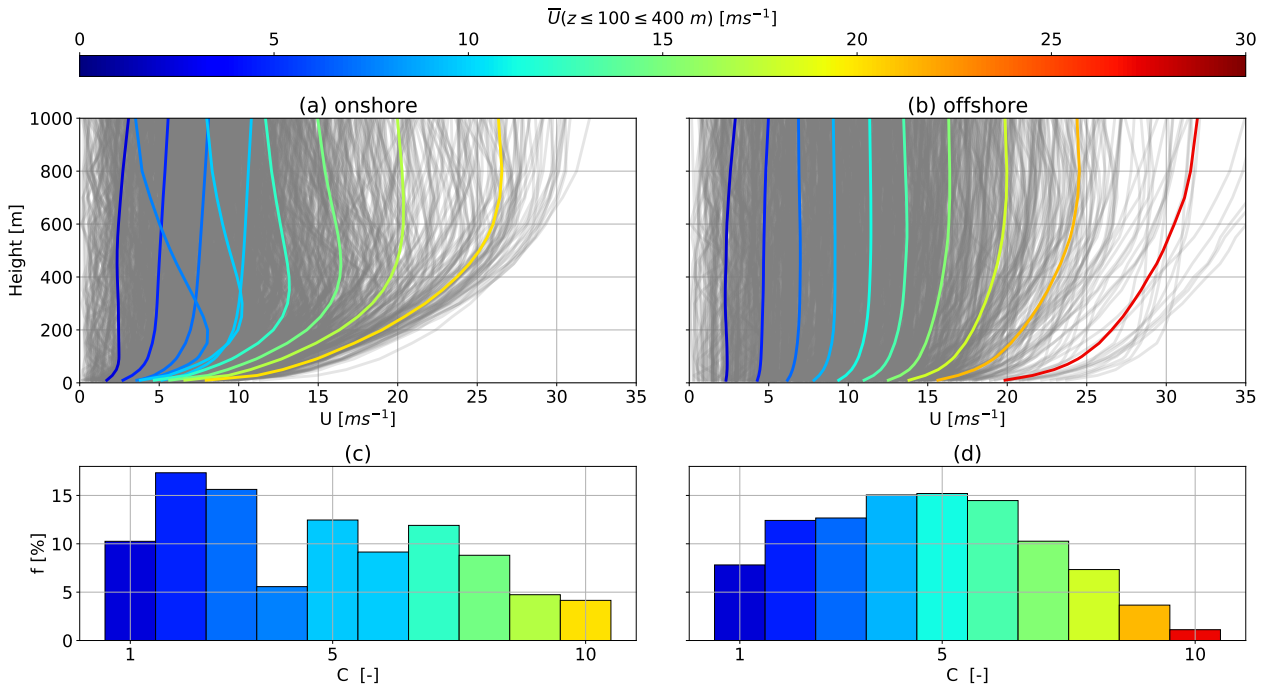

Figure 5. Onshore (left) and offshore (right) average annual wind speed profiles (centroids) resulting from k-means clustering for $k = 10$ (a,b). All comprising WRF-simulated wind speed profiles are depicted in gray. The centroids are sorted, labeled and color coded in ascending order of average wind speed between 100 and 400 m. The corresponding cluster frequency of occurrence f for each cluster C is shown in (c) and (d) below.

As expected, offshore (Figure 5 b) low altitude wind speeds are higher and wind shear is lower than onshore (Figure 5 a). Overall, offshore centroids ~~are~~ wider spread in comparison to the onshore profiles and do not show a wind speed reversal. This

250   indicates more homogeneous wind conditions offshore and a higher likelihood of LLJs onshore. At both locations, the first two clusters exhibit very low wind shear with an almost constant wind speed above 200 m. These low wind speed clusters amount to approximately 25 % onshore (c) and 20% offshore (d), as can be seen in the corresponding cluster frequency of occurrence f. A standard logarithmic wind profile does not accurately describe such almost constant profiles which could lead to an overestimation of wind speeds at higher altitudes. Therefore, AWESs need to be able to either operate under such low

wind speeds or need to safely land and take-off. Onshore clusters 4 and 5 seem to mostly comprise of non-monotonic profiles as these centroids show a distinct LLJ nose at about 200 m and 300 m. Onshore centroids of clusters 7 and 8 also show a slight wind shear inversion at higher altitudes.

Within a cluster, the wind speed profiles span a fairly narrow range of wind speeds indicating coherent clusters. Figure 6 shows the distribution of wind speed profiles within each of the clusters.
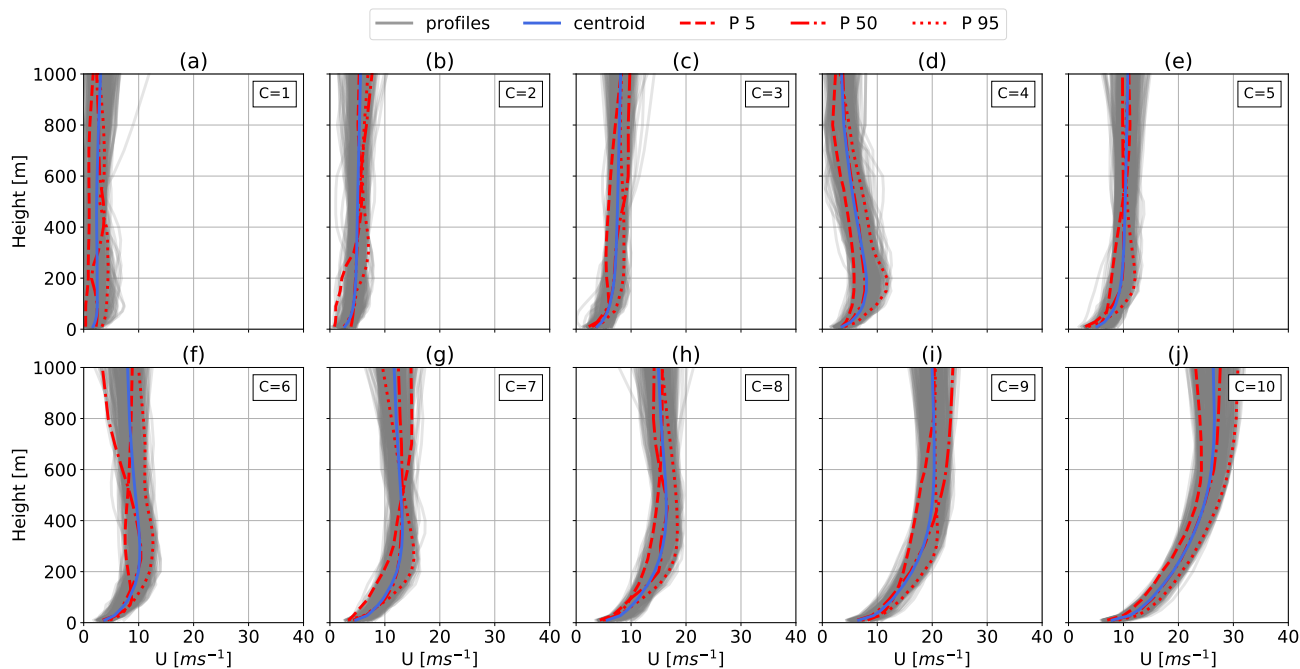
Figure 6. Vertical onshore wind speed profiles categorized into $k = 10$ clustered using the k-means clustering algorithm. Later analyses use $k = 20$ clusters. The average profile (centroid) is shown in blue and the profiles associated with this cluster are shown in gray. Clusters 1 to 10 (a-j) are sorted and labeled in ascending order of average centroid wind speed between 100 m and 400 m. The corresponding cluster frequency f for each cluster C is shown in Figure 5. The red lines mark the wind speed profile with the 5th, 50th and 95th percentiles of average wind between 100 and 400 m within each cluster.

The clusters C = 1 (a) to C = 10 (j) are sorted by average centroid (blue line) wind speed between $U(z_{\mathrm{ref}} = 100 - 400 \text{ m})$. The red lines indicate the profile associated with the 5th, 50th and 95th percentiles of $U(z_{\mathrm{ref}})$ within each cluster. To reduce computational cost, only these profiles are later implemented into the awebox optimization framework. We chose these profiles because they are less likely to be an irregular outliers of their respective cluster than the cluster's extrema. Furthermore, these profiles describe the in-cluster variation with respect to wind speed and profile shape. The focus of this study is the investigation of AWES performance subject to realistic wind conditions, which is why we opted against using averaged or scaled data, such as the cluster centroids or normalized wind speed profiles. The equivalent offshore clusters can be found in Figure A1 in the

appendix. Evidently, the wind speed magnitude plays a dominant role in the clustering process. This can lead to profiles with different shapes to be assigned to the same cluster due to similar average wind speed. A clearer wind profile shape distinction could be achieved by normalizing the data before clustering it (Molina-García et al., 2019; Schelbergen et al., 2020).

## 2.5 Analysis of clustered statistics

This subsection investigates the correlation between clusters and monthly (Figure 7), diurnal (Figure 8) and atmospheric stability (Figure 9) for the onshore (top row) and offshore (bottom row) location. This reveals patterns within the clusters, gives an insight into the wind regime and informs AWES performance for a given time and location. Here only $k = 10$ clusters are chosen for presentation purposes, but wind data from $k = 20$ will be investigated in later sections. Clusters are sorted in ascending order of average centroid wind speed $U(z_{\mathrm{ref}} = 100 - 400 \text{ m})$ and color coded accordingly. The corresponding centroids are shown in Figure 5.

Both locations follow a distinct annual pattern (Figure 7). Profiles associated with high wind speeds are more likely during the winter months and profiles with low wind speeds are predominantly found in summer. The two onshore and offshore clusters associated with the highest wind speed are almost exclusively present during November to February.
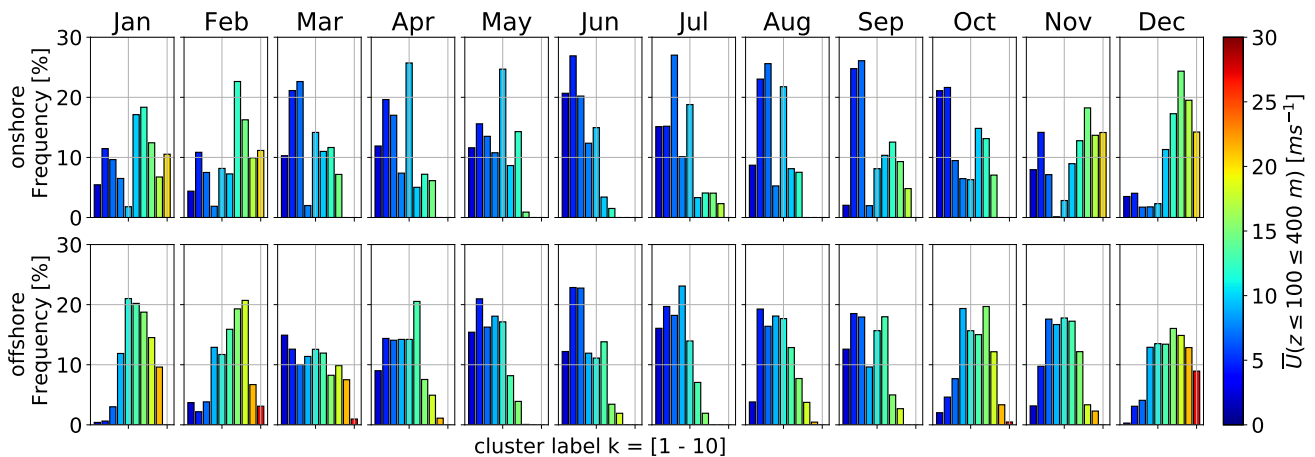
Figure 7. Monthly frequency of k-means clustered onshore (top) and (offshore) wind velocity profiles for a representative $k = 10$. All clusters are sorted and color coded according to their average wind speed between 100 and 400 m. The corresponding centroid associated with each cluster can be found in Figure 5.

Offshore data shows almost no diurnal variation (Figure 8) with only a slight increase of clusters associated with lower wind speeds during daytime. Onshore clusters on the other hand are more dependent on the diurnal cycle with a higher likelihood of low speed clusters after sunrise. The frequency of onshore cluster 4, which comprises a LLJ nose (Figure 5), drops to almost zero during daytime and increases during nighttime, substantiating the assumption that this cluster is associated with nocturnal LLJs.
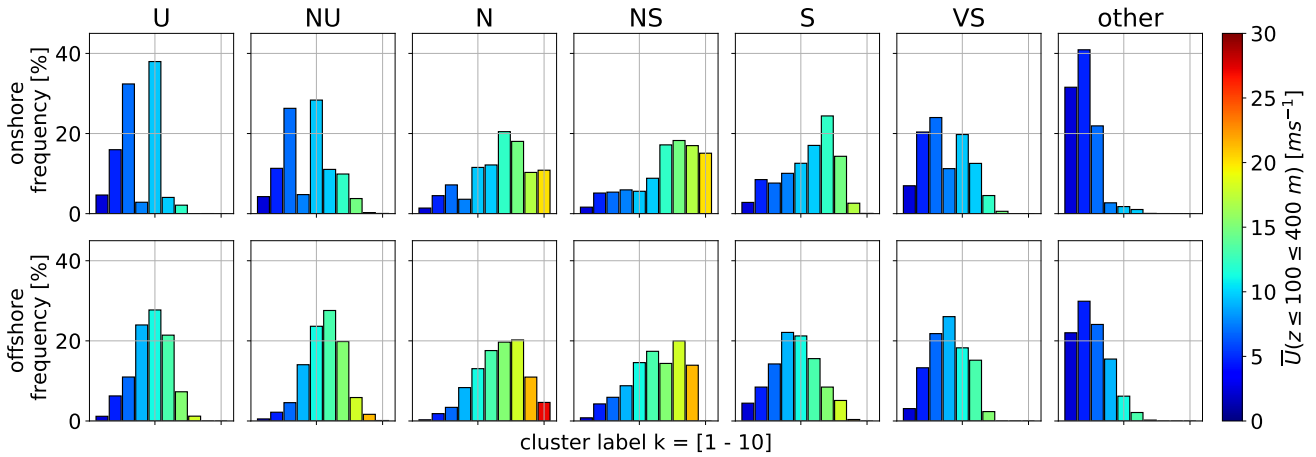
14
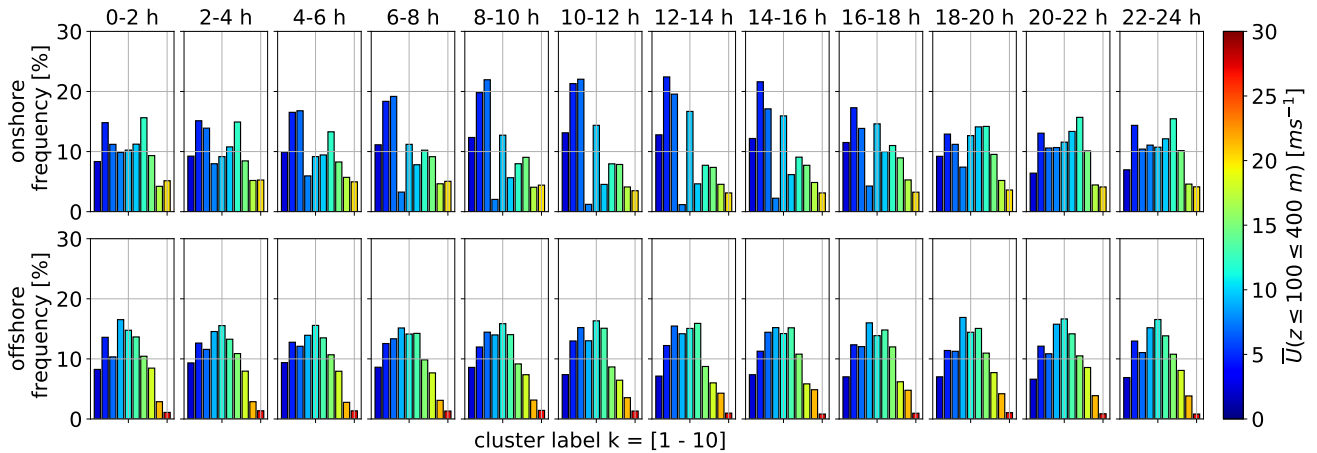
Figure 8. Diurnal frequency of k-means clustered onshore (top) and (offshore) wind velocity profiles for a representative $k = 10$. All clusters are sorted and color coded according to their average wind speed between 100 and 400 m. The corresponding centroid associated with each cluster can be found in Figure 5.

The wind velocity clusters correlate with atmospheric stability as expected (Figure 9). Low wind speed clusters make up about 20% to 30% of the annual wind resource. These clusters exhibit Obukhov lengths close to zero (likely caused by very low friction velocity u_*) and are classified as "other" because they do not fall within one of the other atmospheric stability classes according to (Floors et al., 2011) (Table 2). Unstable (U) and near unstable (NU) conditions are associated slightly higher wind speeds. The highest wind speeds develop during neutral (N) and near stable (NS) conditions. It needs to be acknowledged that strong winds driven by large pressure gradients can lead to neutral stratification. LLJ profiles associated with onshore cluster 4 are most likely to develop during stable (S) and very stable (VS) conditions.

In conclusion, k-means clustering is able to capture and reveal temporal variations in the wind regime as well as location specific wind profile shapes up to high altitudes. Wind speed magnitude seems to determine the resulting clusters more than profile shape. Less common, non-monotonic profile shapes, for example profiles with LLJs, can be identified. Normalizing the profiles before clustering will give more insight into the different vertical profile shapes, but is not pursued in the present study. The cluster frequency reflects the expected temporal and atmospheric stability classification.

3 Dynamic AWES model

This section introduces the dynamic AWES model used in the `awebox` trajectory optimization framework (De Schutter et al., 2020). Sub-section 3.1 gives an overview of the system configuration. The following Sub-sections introduce the aerodynamic model (Sub-section 3.2), the aircraft mass model (Sub-section 3.3).

Figure 9. Atmospheric stability (U: unstable, NU: nearly unstable, N: neutral, NS: nearly stable, S: stable, VS: very stable) distribution of k-means clustered onshore (top) and (offshore) wind velocity profiles for a representative $k = 10$. The associated stability classes are based on Obukhov length (Table 2). All clusters are sorted and color coded according to their average wind speed between 100 and 400 m. The corresponding centroid associated with each cluster can be found in Figure 5.

3.1 Model configuration

The model considers a 6 degrees of freedom (DOF) fixed wing aircraft which is connected to the ground via a straight tether. By introducing the tether, the DOF is reduced to 5, a minimized set of generalized coordinates. It uses precomputed quadratic approximations of the aerodynamic coefficients which are controlled via aileron-, elevator- and rudder-deflection rates (Malz
305 et al., 2019). The longitudinal motion of the tether is controlled via the tether jerk $\dddot{l}$ from which the tether acceleration $\ddot{l}$, reeling speed $\dot{l}$ and length l are determined. The tether is modeled as a single solid rod which cannot support compressive forces nor bending moments (De Schutter et al., 2019). The rod is divided into $n_{\mathrm{aero}} = 10$ segments. Tether drag is calculated individually for each segment, using the local apparent wind speed (Bronnenmeyer, 2018). The tether drag of every segment is equally distributed to the two endpoints and propagated to either the aircraft or ground station. This leads to an underestimation of total tether drag at the aircraft. Refer
310 to (Leuthold et al., 2018) for more details. The ground station itself is not explicitly modeled, but implemented as a set of constraints.

A reel-in speed of $\dot{l}_{\mathrm{in}} = 15 \mathrm{~ms}^{-1}$ and reel-out speed of $\dot{l}_{\mathrm{out}} = 10 \mathrm{~ms}^{-1}$ are chosen, resulting in a reel-out to reel-in ratio of $\frac{2}{3}$ which is assumed to be within design limitations of the winch. A maximum tether acceleration of $\ddot{l} = 20 \mathrm{~ms}^{-2}$ is imposed to comply with generator torque limits. The tether diameter is chosen such that the maximum tether tension is about $F_{\mathrm{tether}}^{\mathrm{max}} =$
315 50 kN with a safety factor of SF = 3. This results in a rated average cycle power of about $P_{\mathrm{rated}} \approx 260 - 300 \mathrm{~kW}$. These ground station and tether constraints do not represent a fully optimized design, but rather an example system.

16

3.2 Aerodynamic model

The presented model utilizes the Ampyx AP2 ~~Power~~ aerodynamic coefficients from De Schutter et al. (2020); Malz et al. (2019); Ampyx (2020). The AP2 reference is scaled to a wing area of $A = 20\ \mathrm{m}^2$ while the aspect ratio is kept constant at $AR = 10$. The total drag coefficient $c_{\mathrm{D,total}}$ [combined] of the aircraft and tether ~~highly~~ [strongly] depends on tether drag and therefore diameter d and length l, as well as the ~~wing~~ [projected surface] area A and aerodynamic drag coefficient ~~of the wing~~ [of the wing] $c_{\mathrm{D,wing}}$. To illustrate the effect of a longer tether, we utilize a simple tether drag estimation and visualize the aerodynamic coefficients for tether lengths up to $l = 1000\mathrm{m}$ in Figure 10.
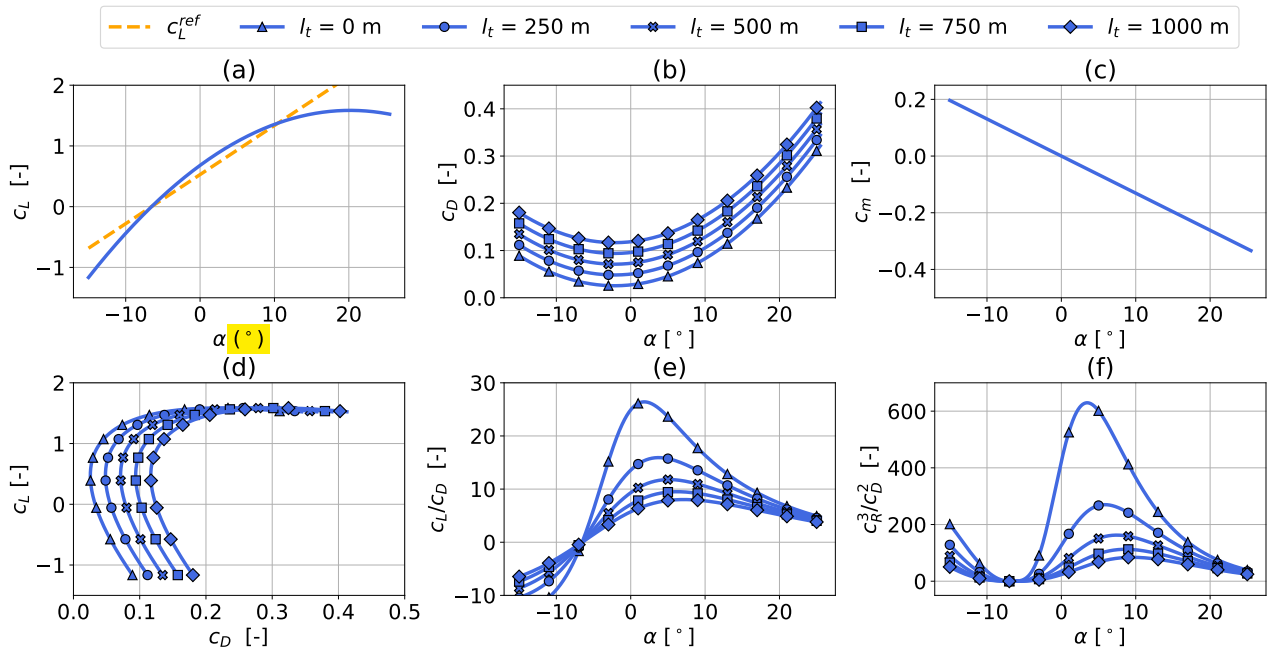
Figure 10. Ampyx AP2 reference wing aerodynamic lift c_{L} (a) and drag $c_{\mathrm{D,total}}$ coefficients (b) (Malz et al., 2019; Ampyx, 2020), including [Power] tether drag according to Equation (2), for a ~~wing area~~ [projected wing surface area] A of $20\mathrm{m}^2$ and tether diameter of $d = 7.8\mathrm{mm}$ (Table 3. Tether length varies between 250 m and 1000 m. (c) shows the pitch moment coefficient c_{m} as a function of angle of attack. The bottom figures display lift over drag (d), lift-to-drag ratio over angle of attack (e) and $c_{\mathrm{R}}^3/c_{\mathrm{D,total}}^2$ over angle of attack (Loyd, 1980).

We consider a straight, cylindrical tether with constant diameter and an aerodynamic ~~tether~~ drag coefficient $c_{\mathrm{D,tether}}$ of 1.0, ~~which would be even higher for braided tethers.~~ Assuming a uniform [constant and] wind [speed], the line integral along the tether results in a total effective drag coefficient of~~:~~

$$c_{\mathrm{D,total}} = c_{\mathrm{D,wing}} + \frac{1}{4}\frac{ld}{A} c_{\mathrm{D,tether}} . \tag{2}$$

See Houska and Diehl (2007); Argatov and Silvennoinen (2013) and van der Vlugt et al. (2019) for details.

We approximate the wing's lift coefficient c_L (Figure 10 a) by a quadratic function to simulate stall effects. A polynomial description for the entire range of AoA is necessary, as the optimization algorithm requires a two-times differentiable function. As a result, the implemented c_L (blue) slightly exceeds the linear (orange) lift coefficient c_L^{ref} between $-5 \leq \alpha \leq 10°$. The pitch moment (Figure 10 c) is assumed to behave linearly and changes in the drag coefficient (Figure 10 b) are approximated by a quadratic function. Tether drag is independent of aircraft angle of attack and therefore added to the zero-lift drag coefficient c_{D0}. c_R is represented as the resultant aerodynamic force coefficient:

$$c_R = \sqrt{c_L^2 + c_{D,\text{total}}^2}. \tag{3}$$

The maximum values of the glide ratio $c_L/c_{D,\text{total}}$ (Figure 10 e) and the ratio $c_R^3/c_{D,\text{total}}^2$ (Figure 10 f) which is one of the main determining factors of AWES power (Schmehl et al., 2013; Loyd, 1980), decrease significantly with tether length and shift towards higher angles of attack. This effect is less pronounced for larger wings because the effect of tether drag reduces when scaling up to larger aircraft.

3.3 Aircraft mass model

The aircraft dynamics are described by a single rigid body of mass m_{aircraft} and moment of inertia $\mathbf{J}$, subject to aerodynamic forces and moments. The inertial properties m_{aircraft} and $\mathbf{J}$ are determined by upscaling the AP2 reference wing from $A_{\text{wing}}^{\text{AP2}} = 3 \text{ m}^2$ to $A = 20 \text{ m}^2$. The Mass m_{scaled} and moment of inertia $\mathbf{J}_{\text{scaled}}$ of a fixed wing aircraft scale as functions of the wing span b with a mass-scaling exponent κ.

$$m_{\text{scaled}} = m_{\text{ref}} \left(\frac{b}{b_{\text{ref}}} \right)^{\kappa}, \tag{4}$$

$$\mathbf{J}_{\text{scaled}} = \mathbf{J}_{\text{ref}} \left(\frac{b}{b_{\text{ref}}} \right)^{\kappa+2}. \tag{5}$$

Pure geometric scaling corresponds to Galileo's square-cube law with $\kappa = 3$. In reality, as has been seen for the development of conventional WTs, design and material improvements occur over time. A review of the available literature containing system mass details was conducted to identify an appropriate mass-scaling factor. The results are shown in Figure 11 depicting actual and anticipated AWES scale bounded by $\kappa = 2.2 - 2.6$ (gray area). We chose $\kappa = 2.4$ based on a curve fit of the available published sizing study data. This seems quite ambitious and might be achievable for soft wing kites. The mass of these hollow tensile structures filled with air mostly scales the wing area, leading to significantly lower mass-scaling exponents and more beneficial mass-scaling. (Sommerfeld et al. (2020)) investigated the effect of variable mass-scaling exponents.

18
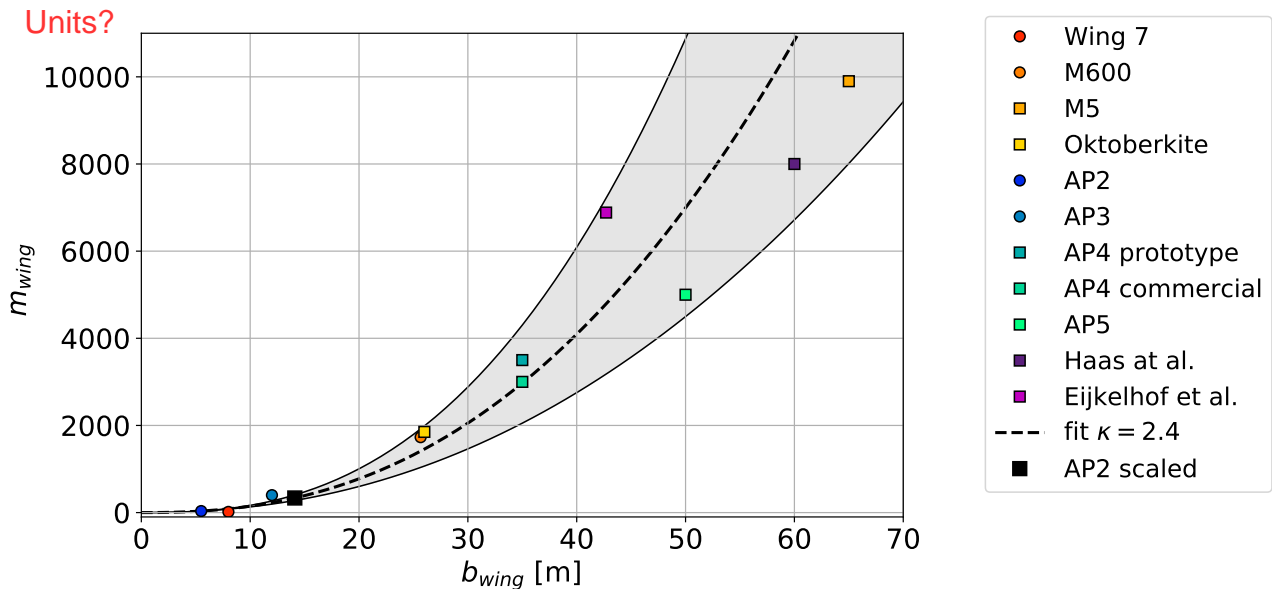
Figure 11. Curve fit of published sizing studies aircraft mass (Haas et al., 2019; Kruijff and Ruiterkamp, 2018; Eijkelhof et al., 2020; Ampyx, 2020; Echeverri et al., 2020). For these data mass scales within a scaling exponent range of $\kappa = 2.2 - 2.6$ (gray area). The chosen mass-scaling exponent of $\kappa = 2.4$ is represented by a dashed line and the investigated scaled AP2 design is highlighted by a black square.

4 Optimal control Model

AWES need to dynamically adapt to changing wind conditions to optimize power generation and ensure save operation. This section introduces the dynamic trajectory optimization awebox toolbox (De Schutter et al., 2020) (Sub-section 4.1) and describes the most important boundary (Sub-section 4.2) and initial conditions (Sub-section 4.3 . Sub-section 4.4 explains the implementation of the previously described wind profiles. A polynomial fit through the simulated data points is needed, as the gradient-based optimizer requires an at least two times differntiable function.

4.1 AWES model overview

Only one production cycle, including reel-in and reel-out, is optimized. Take-off and landing are not considered. Maximizing the average cycle power can be formulated as an trajectory optimization problem which combines the interaction between tether, flying wing and ground station. This study analyzes the mechanical power produced by a single tethered aircraft with a straight tether. Power production is intrinsically linked to the aircraft's flight dynamics, as the AWES never reaches a steady state over the course of a power cycle. Generating dynamically feasible and power-optimal flight trajectories is nontrivial, given the nonlinear and unstable system dynamics and the presence of nonlinear flight envelope constraints. Optimal control methods

are a natural candidate to tackle these problems, given their inherent ability to deal with nonlinear, constrained multiple-input-multiple-output systems (De Schutter et al., 2019; Leuthold et al., 2018). This trajectory optimization is a highly nonlinear
370   and non-convex problem which can have multiple local optima, depending on initialization. The initial and final state of each trajectory are freely chosen by the optimizer but must be equal to ensure periodic operation. In periodic optimal control, an optimization problem is solved by computing periodic system state and control trajectories that optimize a performance index (here average power output $\overline{P}$) while satisfying the system's dynamic equations. We apply this methodology to WRF-simulated wind speed profiles to generate a range of realistic trajectories. The temporal development of important operational parameters
375   is illustrated to better understand instantaneous performance and estimate average cycle power. Any wind data sets, such as wind atlas data, LiDAR or met mast measurements can be implemented into the optimization model via a twice differentiable function, depending on the scope and purpose of the investigation.

4.2   Constraints

Several important constraints define the operational envelop. The most important constraints such as tether length, speed and
380   force are summarized in Table 3. The following constraints define a representative and not optimized AWES design.

The power of ground generation AWES is limited by the tether force, which is defined by the tensile strength ($\sigma_{\mathrm{max}}^{\mathrm{tether}}$) and tether diameter, and the tether speed. The tether diameter is chosen such that the maximum tether tension is about $F_{\mathrm{tether}}^{\mathrm{max}} = 50$ kN with a safety factor of SF = 3. This results a peak power of $P_{\mathrm{peak}} \approx 500$ kW, assuming a maximum reel-out speed of $\dot{l} = 10$ ms^{-1}. This corresponds to a rated average cycle power of approximately $P_{\mathrm{rated}} \approx 260 - 300$ kW. The tether length
385   constraint is very loos, to allow the optimizer to investigate a wide range of possible operating heights. We assume a reel-out to reel-in ratio of $\frac{2}{3}$ to be within winch design limitations. Flight envelope constraints include limitation of aircraft acceleration, roll and pitch angle (to avoid collision with the tether) and angle of attack. Furthermore, a minimal operating height of $z_{\mathrm{min}} = 50 + \frac{A_{\mathrm{wing}}}{2}$ m is imposed for safety reasons.

4.3   Initialization

390   The results generated by the highly nonlinear and non-convex trajectory optimization can have multiple local optima. These solutions, for which only local optimality can be guarantied, depend on the chosen initialization. Some of these local optima can have unwanted characteristics, which is why the quality of all solutions needs to be evaluated a posteriori. To solve this complex problem, initial guesses are generated using a homotopy technique similar to Gros et al. (2013). The homotopy technique initially fully relaxes the dynamic constraints using fictitious forces and moments to reduce model nonlinearity and coupling,
395   improving the convergence of Newton-type optimization techniques. The constraints are then gradually re-introduced until the relaxed problem matches the original problem. The optimization is initialized with a circular trajectory with a fixed number of $n_{\mathrm{loop}} =$ five loops at a 30° elevation angle, an initial tether length $l_{\mathrm{init}} = 500$ m, in positive x direction and an estimated aircraft speed of $v_{\mathrm{init}} = 10$ ms^{-1}. This initialization is kept constant for all wind speed profiles. The number of loops is not part of the objective function and does therefore not change with wind speed. The impact of the number of loops needs to be investigated
400   further, but previous analyses showed that the awebox-estimated average cycle power is rather insensitive to the number of

Table 3. Selected AWES design parameters for the original AP2 reference system (Malz et al., 2019) and the scaled $A = 20$ m^2 design, analyzed in this study. Values in square brackets represent the upper and lower bounds, which are implemented as inequality constraints.

	Parameter	AP2	design 1
	A [m^2]	3	20
	c_{wing} [m]	0.55	1.42
	b_{wing} [m]	5.5	14.1
Aircraft	AR [-]	10	10
	m_{aircraft} [kg]	36.8	355
	α [°]		[-10 : 30]
	β [°]		[-15 : 15]
	l [m]		[1 : 2000]
	$\dot{l}$ [ms^{-1}]		[-15 : 10]
	$\ddot{l}^{\text{max}}$ [ms^{-2}]		[-10 : 10]
Tether	d [mm]		7.3
	$\sigma_{\text{max}}^{\text{tether}}$ [Pa]		3.6×10^9
	SF [-]		3
	z_{min} [m]		60
Operational	α [°]		[-10 20]
	β [°]		[-5 5]

loops. It is likely beneficial to reduce the number of loops with wind speeds because higher wind speeds reel out faster and reach maximum tether length faster.

4.4 Wind profile implementation

This study investigates WRF-simulated wind data, instead of assuming a wind profile relationship such as the logarithmic or exponential wind profile. These relationships do not appropriately represent wind conditions above earth's surface layer (Optis et al., 2016) and cannot emulate the variety of non-monotonic and non-logarithmic wind profiles which occur at both locations. This is particularly important for AWES which can benefit from and need to be able to operate in these conditions.

To reduce the computational cost while maintaining an adequate representation, we only implement three wind velocity profiles from each cluster into the trajectory optimization framework. More profiles could be chosen for an in-depth analysis. A total of 60 profiles, three profiles for each of the k = 20 clusters (Section 2.3), for each location are optimized. The three selected profiles correspond to the 5th, 50th and 95th percentiles of average wind speed $U(z_{\text{ref}} = 100 - 400$ m$)$ within each cluster. We assume that these profiles represent the cluster's spectrum of wind conditions at operating height.

The longitudinal u and lateral v wind components of the sampled WRF-simulated wind profiles are rotated such that the main wind direction u_{main}, defined as the average wind direction between 100 and 400 m, is pointing in positive x-direction

and the transverse component u_{dev} in y-direction. This is equivalent to assuming omnidirectional operation. The `awebox` uses the gradient-based MA57 solver (HSL, 2020) in IPOPT (Waechter and Laird, 2016) to solve the non-linear control problem. Therefore, it is necessary to interpolate the velocity profiles with a twice continuously differentiable function. We chose to use Lagrangian polynomials (Abramowitz and Stegun, 1965) because the resulting polynomials pass through the input data points. To avoid over fitting a limited number of data points are implemented. These data points are chosen based on the anticipated operating height, to best represent the wind conditions at relevant heights.

For comparison, logarithmic wind speed profiles, with a roughness length of $z_0^{\text{onshore}} = 0.1$ and $z_0^{\text{offshore}} = 0.001$, are implemented into the trajectory optimization framework

$$U_{\text{log}} = U_{\text{ref}} \left(\frac{\log_{10}(z/z_0)}{\log_{10}(z_{\text{ref}}/z_0)} \right).$$ (6)

The reference wind speed U_{ref}, at reference height $z_{\text{ref}} = 10\,\text{m}$, varies from 3 to $20\,\text{ms}^{-1}$ with a step size of $\Delta U_{\text{ref}} = 1\,\text{ms}^{-1}$. The `awebox` includes a simplified atmospheric model based on international standard atmosphere to account for air density variation.

5 Reference models

This section introduces reference models used in Section 6 to analyze and contextualize the optimization results. To compare the optimization results to analytic solutions, we define a quasi-steady-state AWES reference model (QSM) (Sub-section 5.1) and a steady-state WT model (Sub-section 5.2).

5.1 AWES reference model

The QSM estimates the mechanical power of ground-generation AWES based on the assumption that the trajectory of the tethered aircraft can be approximated by a progression through steady equilibrium states where tether tension and total aerodynamic force are aligned. The QSM, based on Argatov et al. (2009) and generalized by Schmehl et al. (2013), approximates the aircraft as a point mass. Its position is described in the spherical coordinates by the distance from the ground station, the elevation angle ε and azimuth angle ϕ relative to the wind velocity vector U. For lightweight kites, this is a reasonably good approximation because the low mass of the kite leads to very short acceleration times. The model includes losses caused by the misalignment of the tether and wind velocity vector. The same model parameters and constraints of the optimization model also apply to the QSM reference model (see Sub-section 4.2).

The average cycle power P_{QSM} can be estimated from the reel-out power P_{opt}, the power losses during reel-in P_{in}:

$$P_{\text{QSM}} = P_{\text{out}}\, t_{\text{out}} - P_{\text{in}}\, t_{\text{in}} = P_{\text{out}}\, \frac{\dot{l}_{in}}{\dot{l}_{out} + \dot{l}_{in}} - P_{\text{in}}\, \frac{\dot{l}_{out}}{\dot{l}_{out} + \dot{l}_{in}}.$$ (7)

We assume reel-in power losses P_{in} to be zero because optimal reel-in tether tension is negligible. This reduces the average cycle power by up to 30%, depending on wind speed. Due to the cyclic nature of the trajectory, we can determine the ratio of

the reel-in time t_{in} and reel-out time t_{out} to the total cycle time from the reel-in speed $\dot{l}_{in}$ and reel-out speed $\dot{l}_{out}$. $\dot{l}_{out}$ depends on the wind speed, while the $\dot{l}_{in} = -15\,\text{ms}^{-1}$ is assumed to be the maximum reel-in speed. We assume a constant tether force F_{tether} and tether speed during reel-in and reel-out. The transition time between both phases is neglected. P_{out} is calculated from the product of tether speed $\dot{l}$ and tether tension F_{tether}:

$$P_{\text{out}} = F_{\text{tether}}\,\dot{l}_{\text{out}} = \frac{\rho_{\text{air}}}{2} A v_{\text{app}}^2 c_{\text{R}} \left(\frac{c_{\text{R}}}{c_{\text{D,total}}} \right)^2 \dot{l}_{\text{out}}. \tag{8}$$

Tether tension is a function of wind speed magnitude U, air density ρ_{air} and the resultant aerodynamic force coefficient c_{R} (Equation (3)), which is calculated from the aerodynamic lift c_{L} and total drag coefficient $c_{\text{D,total}}$ (Equation (2)), including wing and tether drag. The tether speed $\dot{l}$ is non-dimensionalized in the form of the reeling factor:

$$f = \frac{\dot{l}}{U}, \leq \cos\varepsilon \cos\phi. \tag{9}$$

which is constrained by the elevation ε and azimuth angle ϕ as the magnitude of the apparent wind speed cannot be negative. Combining equations (8) and (9) results in:

$$P_{\text{out}} = \frac{\rho_{\text{air}}}{2} A U^3 c_{\text{R}} \left(\frac{c_{\text{R}}}{c_{\text{D,total}}} \right)^2 f \left(\cos\varepsilon \cos\phi - f \right)^2. \tag{10}$$

The optimal reeling factor is $f_{\text{opt}} = \frac{1}{3}\cos\varepsilon\cos\phi$ which can be derived from Equation (10) by a simple extreme value analysis. F_{tether} is constrained by the tether diameter d, the tensile strength $\sigma_{\text{max}}^{\text{tether}}$ and the safety factor SF.

$$F_{\text{tether}} \leq \frac{d^2}{4} \pi \sigma_{\text{max}}^{\text{tether}} \tag{11}$$

The same sampled WRF-simulated wind profiles (Section 2, Sub-section 2.3) as implemented into the dynamic optimization framework are also investigated using the QSM. We maximize cycle average power P_{QSM} by varying l, $\dot{l}$ and z and assuming optimal $\frac{c_{\text{R}}^3}{c_{\text{D,total}}^2}$. The aircraft is assumed to move directly crosswind with a zero azimuth angle ϕ relative to the wind direction.

5.2 WT reference model

This section introduces a simple steady-state WT model to contextualize the AWES performance. WT power is estimated by:

$$P_{\text{WT}} = \frac{1}{2} \rho_{\text{air}} c_{\text{p}}^{\text{WT}} A_{\text{WT}} U^3 (z_{\text{WT}} = 100\ \text{m}) \tag{12}$$

with a hub height of $z_{\text{WT}} = 100\,\text{m}$ for both onshore and offshore. The rotor diameter $D_{\text{WT}} \approx 26.9\,\text{m}$ is sized such that an equivalent rated power of $P_{\text{rated}} = 260\,\text{kW}$ is reached at a rated wind speed of $v_{\text{rated}}(z_{\text{WT}} = 100\ \text{m}) = 12\ \text{ms}^{-1}$, assuming a constant power coefficient of $c_{\text{p}}^{\text{WT}} = 0.45$. The power is kept constant above rated wind speed. Performance is compared based on the same sample of WRF-simulated wind speed profiles.

6 Results and discussion

This section analyses the optimization results and compares them to the reference models. Sub-section 6.1 investigates power-optimal trajectories and the time series of important operational parameters. Sub-section 6.2 examines operating height statistics, tether length and elevation angle trends. Sub-section 6.3 visualizes the impact of difference reference heights on a power curve approximation by comparing average cycle power over $U(z_{\mathrm{ref}} = 100\text{ m})$, $\overline{U}(z_{\mathrm{ref}} = z_{PTH})$ and an apriori guess of the wind speed at pattern trajectory height $\overline{U}(100\text{ m} \leq z_{\mathrm{ref}} \leq 400\text{ m})$. Lastly, Sub-section 6.4 compares the average cycle power based on simulated WRF wind conditions to logarithmic wind speed profiles and contextualizes the data by comparing them to QSM and WT power. All results are subject to the constraints and design parameters introduced in Sections 3 and 4 and do not represent general ground generation AWES.

### 6.1 Flight trajectory and time series results

Figure 12 compares power-optimal flight trajectories for a range of onshore wind conditions. The reference wind speed mentioned in the legend is the apriori guess at the pattern trajectory height $U_{\mathrm{ref}} = \overline{U}(100\text{ m} \leq z_{\mathrm{ref}} \leq 400\text{ m})$. These results have been chosen to visualize typical optimized trajectories for realistic wind conditions. [determined with awebox]

Figure 12 (a) shows the wind speed U over altitude z. Figure 12 (c) shows the corresponding top view of the wind velocity profiles, rotated such that u_{main} points in positive x direction. The WRF-simulated wind profiles are shown in gray. The highlighted segments depict the Lagrangian polynomial fit (Abramowitz and Stegun, 1965) at operating heights, which sufficiently fits the wind data. Figures 12 (b) and (d) show a side ($x - z$ plane) and top view ($x - y$ plane) of the optimized trajectories The optimization predicts an increase in tether length and stroke length with wind speed. Similar results for the offshore location can be found in Figure A2 in the appendix.

Figure 13 illustrates the corresponding temporal development of important operational parameters.

The optimizer maximizes tether tension (Figure 13 (a)) during reel-out even for lower wind speed and adjusts the reel-out speed (Figure 13 (c)) to maximize average cycle power. This increases the reeling factor beyond its optimal value of $f_{\mathrm{opt}} = \frac{1}{3}\cos\varepsilon\cos\phi$ and increases power with wind speed even though the maximum tether force is reached. The resulting instantaneous power is shown in Figure 13 (e). The low wind speed example $U_{\mathrm{ref}} = 5.4\text{ms}^{-1}$ (blue) seems to be just above cut-in wind speeds. Its tether speed drops to zero for an extended amount of time during the reel-out phase to maintain sufficient lift to keep the aircraft aloft. The production period remains almost constant ($t \approx 60\text{sec}$) for the moderate and high wind speed trajectories (orange, green and red), while the reel-in period increases with wind speed, due to the increased reel-out length caused by a higher average reel-out speed. Significant power losses only occur during the transition between the production and retraction phases. During the reel-in phase the tether speed is maxed out while tether tension drops to zero and the aircraft reduces its angle of attack (Figure 13 (d)) to reduce lift. At higher wind speeds the optimizer increases the elevation angle and reduces angle of attack to stay within the constraints. This can result in odd or unexpected trajectories, even though these local minima are feasible solutions within the system constraints. Tether length

24
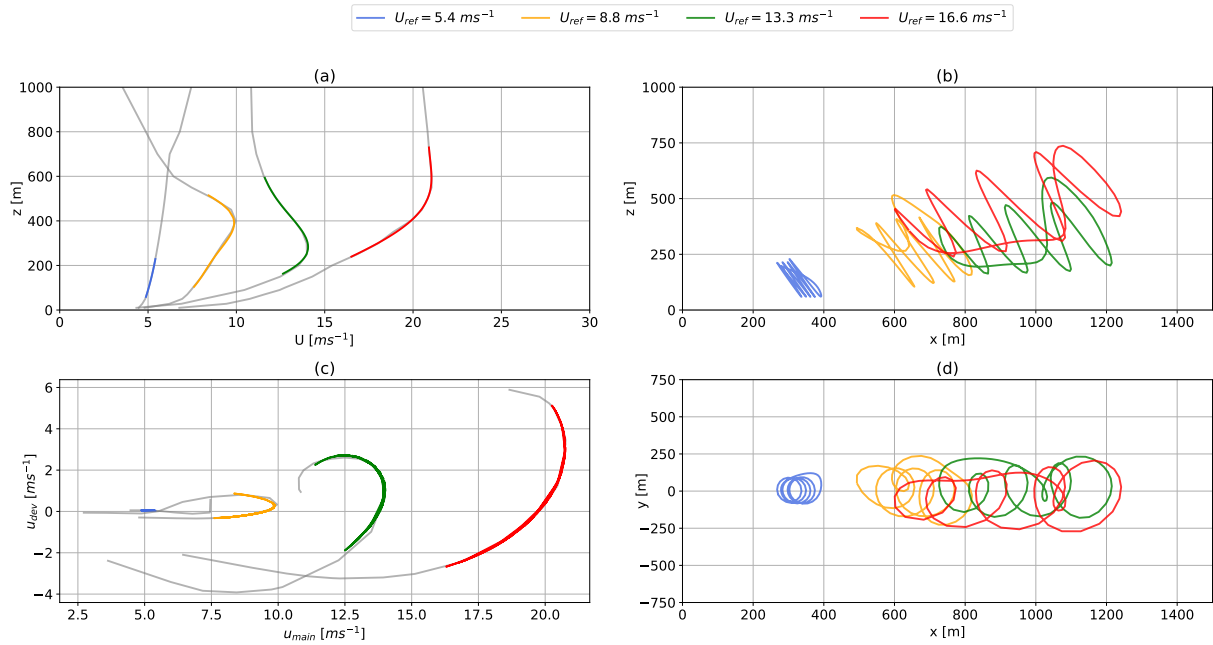
Figure 12. Exemplary onshore trajectories. Wind data are based on sampled WRF-simulated clusters (Section 2). Wind speed magnitude [Vertical wind speed profiles] (a), and hodograph (top view) of wind velocity up to 1000 m (c). The highlighted [trajectory] sections indicate operating wind conditions [highlighted by coloring]. Panel (b) and panel (d) shows the side and top view of the corresponding awebox-optimized trajectories. The reference wind speed in the legend is $U_{\mathrm{ref}} = \overline{U}(100\,\mathrm{m} \le z_{\mathrm{ref}} \le 400\,\mathrm{m})$. The results correspond to the time series shown in Figure 13.

(Figure 13 (f)) generally increases with wind speed as the system reels out faster, increases its elevation angle and operates at higher altitude. Similar results for the offshore location can be found in Figure A3 in the appendix.

6.2 Tether length, elevation angle and operating altitude

This sub-section compares tether lengths l, elevation angles ε and operating heights $z_{\mathrm{operating}}$ resulting from the trajectory optimization of 60 wind velocity profiles from $k = 20$ clusters. Figure 14 (a) illustrates the range of onshore (blue) and offshore (orange) tether lengths l for each wind velocity profile. The maxima and minima are highlighted by circles and plotted over reference wind speed $\overline{U}(z_{\mathrm{ref}} = 100 - 400\,\mathrm{m})$.

None of the optimizations max out the tether length constraint of $l^{\mathrm{max}} = 2000\,\mathrm{m}$. Both locations show a trend towards longer tether lengths up to rated wind speed, where the reel-out speed and tension are almost constant and close to maximum (Figure 13). A longer tether is not beneficial as the AWES needs to stay within design constraints and the additional drag and weight would only reduce performance. The maximum tether length remains almost constant above rated wind speed while the minimum tether length increases slightly, reducing the total stroke length. The elevation angle (Figure 14 (b)) decreases

25
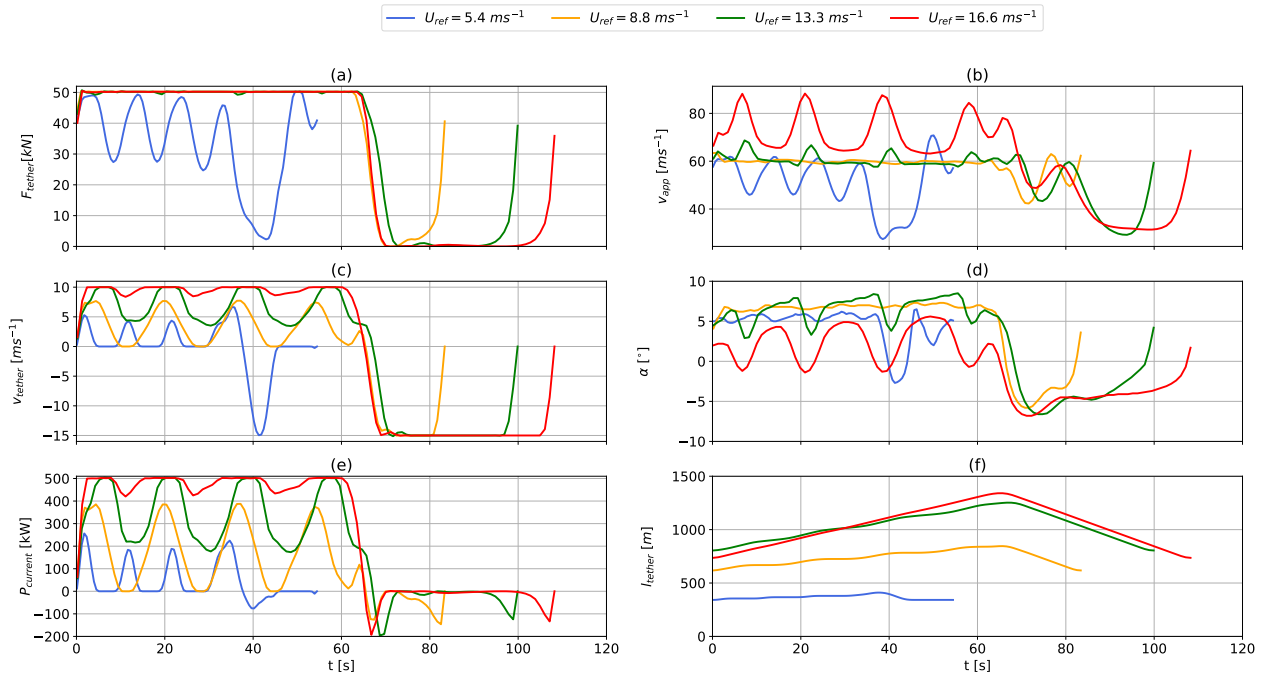
Figure 13. Time series of instantaneous tether tension (a), apparent wind speed (b), tether-reeling speed (c), angle of attack α (d), power (e) and tether length (f). The results correspond to the trajectories, based on sampled onshore WRF-simulated wind data, shown in Figure 12.
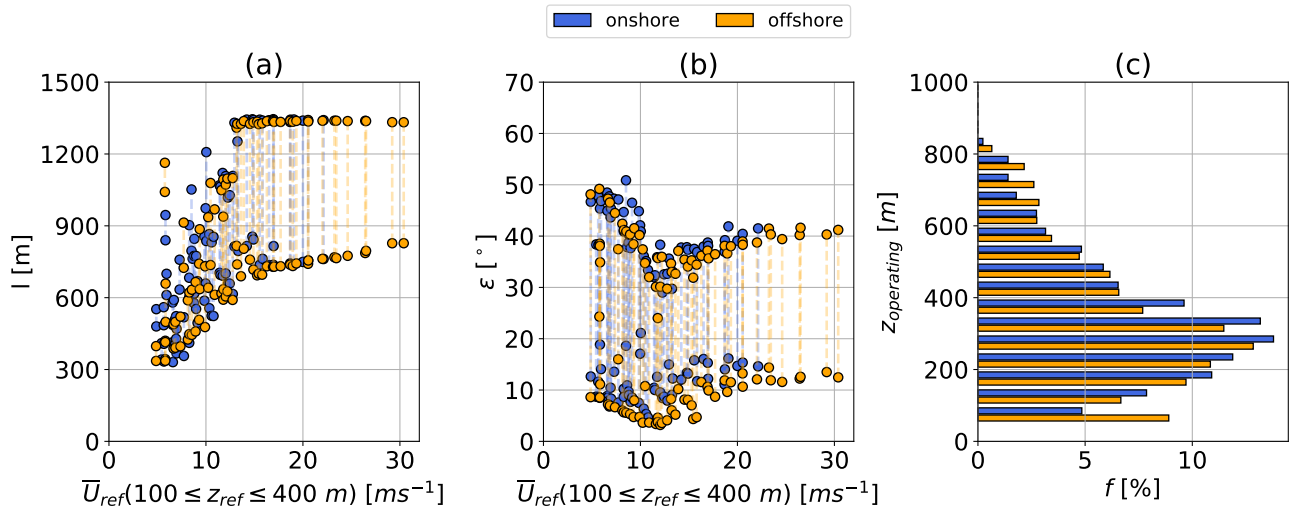

Figure 14. Tether length range (a) over reference wind speed $U(z_{\mathrm{ref}} = 100 - 400 \text{ m})$ and frequency distribution of operating altitude (b) based on `awebox` trajectory optimization of $k = 20$ onshore (blue) and offshore (orange) clusters.

26

as the tether length increases. The optimizer tries to keep the elevation angle low in order to reduce misalignment (cosine) losses between the tether and the horizontal wind velocity vector. The ~~onshore~~ elevation angle is slightly higher due to the [for onshore conditions]

515 higher wind shear which justifies higher operating altitudes. This can also be seen in Figure 14 (c) which shows the frequency distribution of operating altitude $z_{\mathrm{operating}}$. 78.6 % onshore and 74.7 % offshore the optimal operating heights are below 400 m, confirming the findings in Sommerfeld et al. (2019a, b). Larger or multi-kite AWES could benefit from higher operating altitudes due to their higher lift to tether drag ratio and weight ratio, but more detailed analyses are required.

6.3 Impact of reference height on power curve

520 The power curve of wind energy converters ~~depicts~~ [quantifies / specifies] the ~~average~~ power ~~over~~ [that can be harvested at a given] reference wind speed$_{\mathrm{s}}$. For conventional WT the wind speed at hub-height is commonly used as reference wind speed. Whether this is appropriate for ever growing towers an[d] longer ~~WT~~ [rotor] blades is debatable. [De]fining a reference wind speed for AWES is not trivial, as ~~they change their~~ [the] operating height ~~with~~ [range changes with the] wind speed, during each cycle and dependent on wind speed profile ~~shape~~ [the shape of the vertical] [s]. The choice of reference wind speed impacts the power curve representation. The AWE Glossary (Airborne Wind Europe, 2021) recommends to use the wind speed

525 at pattern trajectory height z_{PTH}, which is the expected or logged time-averaged height during the power production phase, as reference wind speed. We estimate $100\,\mathrm{m} \leq z_{\mathrm{ref}} \leq 400\,\mathrm{m}$ as an apriori guess of the wind speed at pattern trajectory height. We do not claim to define a general power curve, but rather investigate the ~~variaton~~ [variation] of average cycle power caused by realistic wind profiles. Figure 15 compares onshore (a) and offshore (b) average cycle power over $U(z_{\mathrm{ref}} = 100\,\mathrm{m})$ (blue), $\overline{U}(z_{\mathrm{ref}} = z_{PTH})$ (green) and an apriori guess of the wind speed at pattern trajectory height $\overline{U}(100\,\mathrm{m} \leq z_{\mathrm{ref}} \leq 400\,\mathrm{m})$ (orange).
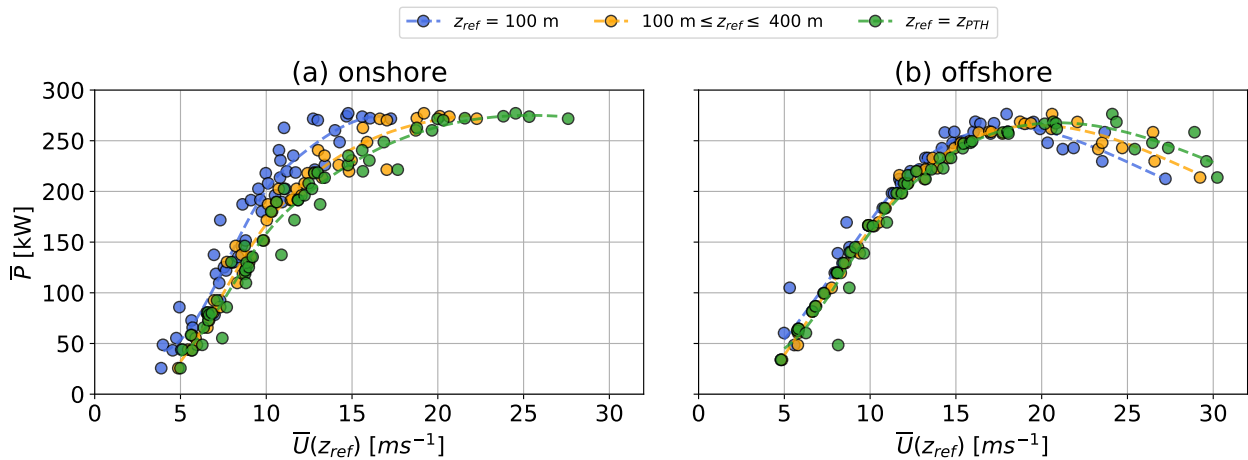
Figure 15. Onshore (a) and offshore (b) AWES power curve$_{\mathrm{s}}$ ~~approximations over wind speed~~ at $z_{\mathrm{ref}} = 100\,\mathrm{m}$ (blue), $100\,\mathrm{m} \leq z_{\mathrm{ref}} \leq 400\,\mathrm{m}$ (orange) and $z_{\mathrm{ref}} = z_{\mathrm{PTH}}$ (green) reference height$_{\mathrm{s}}$. The dashed lines are least-square spline interpolation with a knot at $U_{\mathrm{ref}} = 13\,\mathrm{ms}^{-1}$.

530 The data points correspond to the clustered and sampled WRF-simulated wind speed profiles. The dashed lines, which are only added as visual aid, are a least-square spline interpolation of the approximately 60 data points with a knot at $U_{\text{ref}} = 12\,\text{ms}^{-1}$. This spline definition is chosen to account for the difference in power up to and above rated wind speed.

From these results we conclude that The choice of reference height is more significant onshore. The onshore wind conditions with their higher number of non-monotonic wind speed profiles and higher wind shear lead to ~~more fluctuation~~ larger deviations from the typical power curve shape. The higher

535 wind shear onshore leads to a shift towards lower wind speeds for a reference height of $z_{\text{ref}} = 100$ m. The apriori pattern trajectory height guess of $100\,\text{m} \leq z_{\text{ref}} \leq 400\,\text{m}$ is relatively close to the actual z_{PTH}, especially for lower wind speeds. At very high wind speeds above $\overline{U}_{\text{ref}} \geq 20\,\text{ms}^{-1}$ the z_{PTH} power shifts towards higher wind speeds indicating a~~n~~ ~~higher~~ increased operating ~~altitude~~ height.

The more homogeneous offshore wind conditions result in less power variation. The three different reference heights have

540 almost no impact on the offshore power curve up to the rated wind speed. Above $\overline{U}_{\text{ref}} \geq 20\,\text{ms}^{-1}$ the power curves diverge and the average cycle power decreases. This seems to be a result of the `awebox` optimization and its initialization with a fixed number of loops. As the wind speed and reel-out speed increase, the aircraft cannot complete all the loops before reaching the maximum tether length and transitioning into reel-in. Therefore, one of the loops is performed ~~during the~~ when already reel-in ing, leading to an increase in tether tension (Figure 16 (a)) and additional losses during the reel-in period (Figure 16 (e)). The corresponding

545 trajectories are shown in Figure A4 in the appendix.
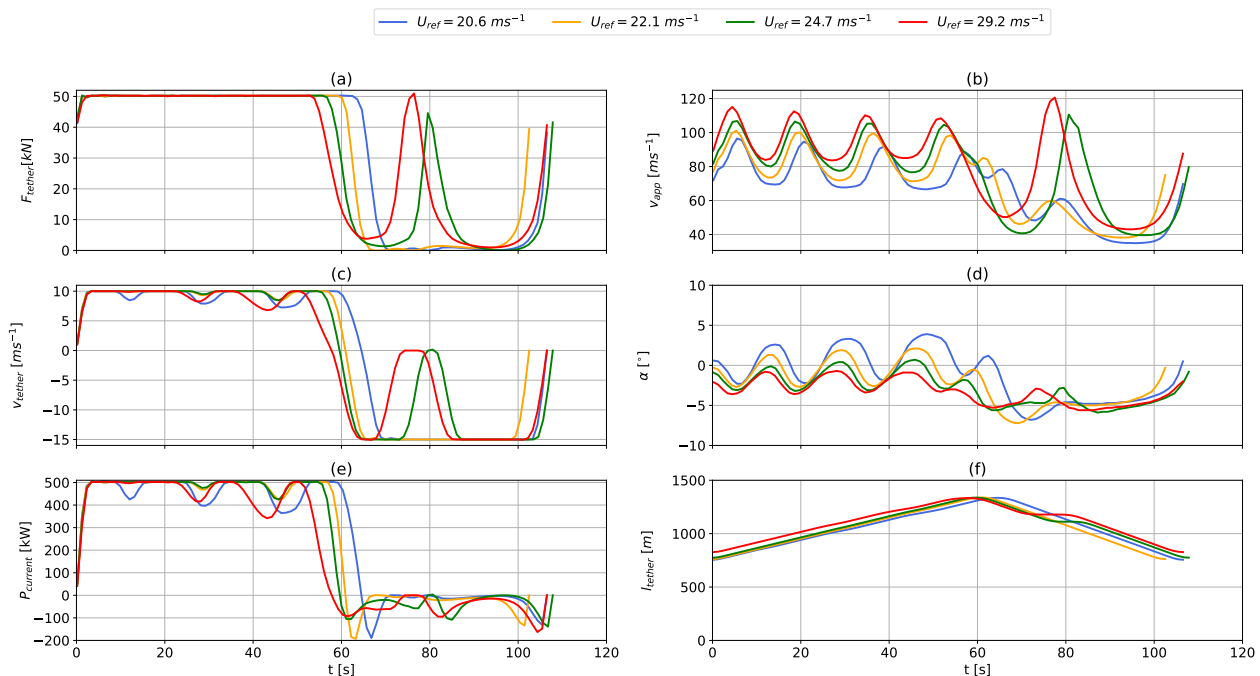
Figure 16. Time series of instantaneous tether tension (a), apparent wind speed (b), tether-reeling speed (c), angle of attack ~~α~~ (d), power (e) and tether length (f) for high speed WRF-simulated offshore wind conditions. The results correspond to the trajectories shown in Figure A4.

6.4 Reference model power comparison

Figure 17 presents the impact of the wind speed profile shape on optimized average cycle power $\overline{P}$ over $\overline{U}_{\text{ref}}(100 \text{ m} \leq z_{\text{ref}} \leq 400 \text{ m})$, by comparing power estimates based on sampled WRF-simulated wind data (blue) to power estimates based on standard logarithmic wind speed profiles (red). These results are verified against the QSM (Sub-section 5.1, orange) and WT reference models (Sub-section 5.2, green).
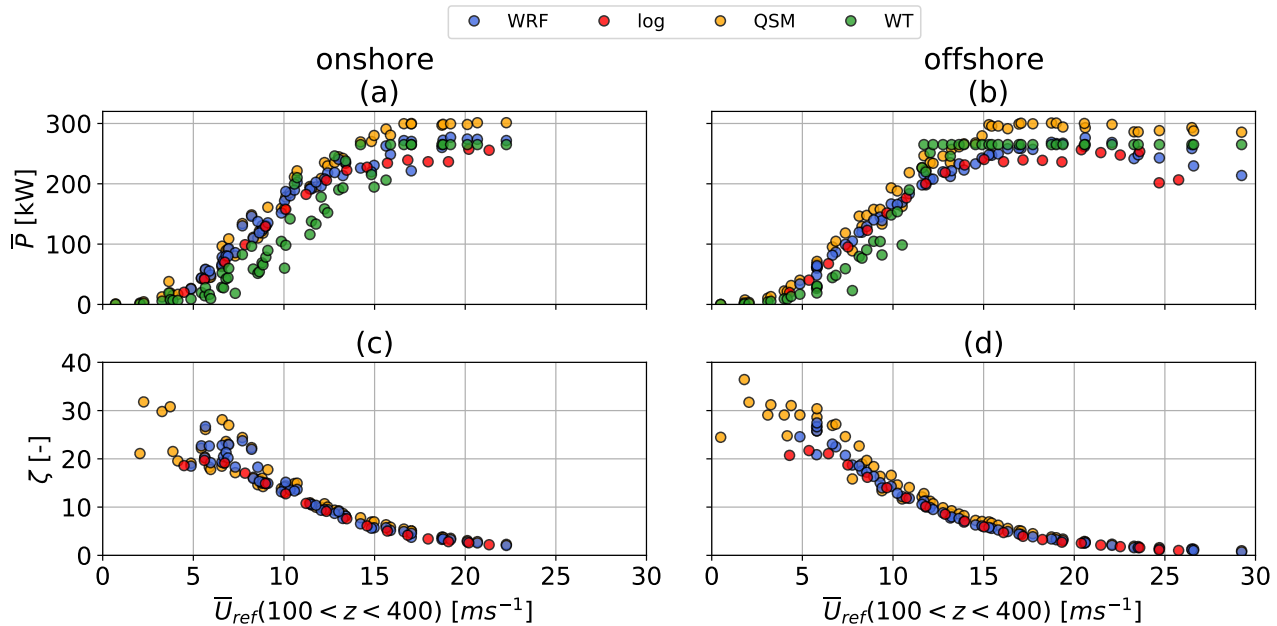
Figure 17. Onshore (a) and offshore (b) average cycle power $\overline{P}$ ~~over~~ as a function of average wind speed between 100 and 400 meters. WRF (blue) data, based on ~~3~~ three wind speed profiles for each of the $k = 20$ clusters, is compared to standard logarithmic wind speed profiles (red). QSM (orange) and WT (green) which use the same sampled WRF profiles are added for reference. The onshore (c) and offshore (d) power-harvesting factor ζ is added as an performance indicator.

No cut-out wind speed is defined. The cut-in wind speed of $\overline{U}_{\text{ref}} \approx 5 \text{ ms}^{-1}$ is the result of unconverged optimizations below this threshold, indicating that the wind is insufficient to keep the AWES aloft. The QSM and WT model estimate power for these wind speeds. Rated power is achieved around $U_{\text{rated}} \approx 12 - 15 \text{ms}^{-1}$, depending on the wind speed profile shape. At this wind speed the reel-out speed is almost constant while a constant reel-out tension is already achieved at lower wind speeds (Figure 13).

The logarithmic wind speed profiles (Equation (6)) use ~~a~~ roughness lengths ~~of~~ between $z_0^{\text{onshore}} = 0.1$ and $z_0^{\text{offshore}} = 0.001$ (Sub-section 4.4). As expected, logarithmic power estimates do not fluctuate as much as the WRF-simulated power. The predicted logarithmic onshore power (Figure 17 (a)) is often slightly below WRF which ~~could~~ would indicate that these WRF profiles exhibit narrow areas of higher wind speeds, such as LLJs. Offshore, the logarithmic and WRF data are in good agreement with the

logarithmic results as most of the simulated wind profiles are more monotonic. At both locations, the higher WRF power above $U_{\mathrm{ref}} \geq 15 \text{ ms}^{-1}$ is likely caused by higher than logarithmic wind shear. However, another contributing factor is the `awebox` optimization and initialization with a fixed number of loops which can lead to loops being performed during the reel-in period which leads to a reduction in average cycle power. Additionally, determining a dynamically feasible and power-optimal trajectory becomes more difficult at higher wind speeds, due to tether speed and tension constraints.

The power-harvesting factor ζ (Diehl, 2013) is an AWES performance metric. It expresses the harvested power P relative to the wind power P_{area} through an area A. Here the average wind speed between $\overline{U}_{\mathrm{ref}}(100 \leq z_{\mathrm{ref}} \leq 400 \text{ m})$ is used to calculate P_{area}, which is not a physical power, but a mathematical concept flux non-dimensionalize power.

$$\zeta = \frac{P}{P_{\mathrm{area}}} = \frac{P}{\frac{1}{2}\rho_{\mathrm{air}} A U_{\mathrm{ref}}^3} \tag{13}$$

ζ can be derived from (8) by setting the elevation angle ε and the azimuth angle ϕ to zero. An extreme value analysis results in an optimal reel-out speed $\dot{l} = 1/3\, U$ (Equation (9)) and $\zeta_{\max} = \frac{4}{27} c_{\mathrm{R}} \left(\frac{c_{\mathrm{R}}}{c_{\mathrm{D}}} \right)^2$.

Both onshore (Figure 17 (c)) and offshore (Figure 17 (d)) show similar trends in agreement with the QSM. ζ decreases with wind speed because tether tension and speed constraints need to be satisfied. Both the QSM and WT reference model use the same sampled WRF-simulated wind data. WT power fluctuates significantly due to the choice of reference height. AWESs outperform WTs up to rated wind speed, particularly onshore where AWESs can take advantage of higher wind speeds aloft. Lower wind shear offshore reduces the need to operate at higher altitudes, reducing the benefit of AWESs. As expected, the QSM predicts the highest power due to the simplified model and assumptions such as constant reel-out and reel-in power and neglected mass.

7 Conclusions and outlook

This study describes optimal single-aircraft, ground generation AWES performance based on sampled mesoscale WRF-simulated wind data by analyzing trajectories, instantaneous performance, operating heights and average cycle power. Throughout the paper an apriori operating heights guess of $100 \leq z_{\mathrm{ref}} \leq 400 \text{ m}$ is used. This guess is verified by comparing the power curve approximations over wind speed at different reference heights. These analyses use one year of onshore wind data at Pritzwalk in northern Germany and one year of offshore wind data at the FINO3 research platform in the North Sea to drive the `awebox` optimization framework, which determines dynamically feasible, power-optimal trajectories. The model uses a scaled Ampyx AP2 aircraft with a wing area of $A = 20 \text{ m}^2$ and is subject to realistic constraints. The annual wind data set is categorized into $k = 20$ clusters using k-means clustering algorithm. To reduce the computational cost, only three wind speed profiles per cluster are implemented into the optimization model. These profiles are sampled based on the 5th, 50th and 95th percentile of wind speed between $\overline{U}_{\mathrm{ref}}(100 \leq z_{\mathrm{ref}} \leq 400 \text{ m})$ to represent the in-cluster variation. Optimal average cycle power is compared to a quasi-steady-state AWES model and a steady-state WT model.

The optimization model is able to determine power-optimal trajectories for complex, non-monotonic wind speed profiles. The results are only slightly lower than the QSM predictions, which assume constant reel-out power, no reel-in power losses and neglect gravity. The predicted AWES power exceeds the WT reference model onshore because it can utilize the higher wind shear and can operate at high wind speed altitudes such as LLJ noses. These conditions are not represented by logarithmic wind speed profiles which is why the average power is generally lower than for WRF-simulated wind. Offshore wind conditions, which are more monotonic and have less wind shear, produce similar average power as their logarithmic approximation. Due to the initialization with a fixed number of maneuvers, high wind speed trajectories show loops during the reel-in period which reduces the average cycle power. The number of loops is currently not a variable in the objective function for the awebox. This can lead to a deterioration of the trajectory at high wind speeds, as the optimizer struggles to stay within the tether tension and tether speed constraint.

An investigation of the instantaneous performance shows that the optimizer first maximizes tether tension and adjusts reel-out speed and angle of attack. With increasing wind speed the tether reel-out speed becomes more constant and approaches the maximum reel-out speed constraint. Up to rated wind speed, when average tether tension and tether speed are maximized, the optimizer increases the deployed tether length and reduces the elevation angle to operate at optimal height. At higher wind speeds, the elevation angle increases to de-power the system and stay within design constraints. As a result, approximately 75 % of the optimal onshore and offshore operating heights are below 400 m. This informs airspace regulators and companies to address the airspace restriction challenge and weakens the claim in early airborne wind energy literature of the substantial energy potential of high altitudes above 500 m. The onshore power curve estimation, using the average wind speed between $100 \leq z_{\mathrm{ref}} \leq 400$ m as reference wind speed, slightly overestimates power compared to the wind speed at pattern trajectory height, which is the expected or actual time-averaged height during the reel-out phase. Offshore, the power curve seems independent of reference height due to lower number of non-monotonic wind speed profiles and lower wind shear.

The mesoscale wind simulations, which comprise one year of wind data with a temporal resolution of 10 minutes at both locations, are categorized and analyzed. The annual wind roses for heights of 100 and 500 m confirm the expected wind speed increase and clockwise rotation at both locations. Offshore shows a lower wind shear and veer than onshore. Annual wind speed statistics reveal that low wind speeds still occur at a fairly high probability up to 1000 m at both locations. The k-means clustering algorithm is able to categorize the wind regime and identify LLJs as well as various non-logarithmic and non-monotonic wind profiles. The main deciding factor seems to be the wind speed, while the profile shape seems to play a less important role. Individual clusters produce coherent groups of similar wind profiles whose probability correlates with seasonal, diurnal and atmospheric stability variation. k-means clustering provides good insight into the wind regime, especially for higher altitudes where classification by Obukhov length is inadequate.

To follow up on this research the AEP could be derived from realistic wind conditions. AWES power curves and their reference wind speed also need to be investigated further, for example by comparing normalized wind speed profiles including the correlation between wind speeds at different reference heights. Future work could analyze the impact of different number of initialization maneuvers or include the number of loops as a variable in the objective function of the optimization. Using the same data and model, it is possible to investigate the annual and diurnal AWES power variation in comparison to WT performance. A

parallel sizing study (Sommerfeld et al., 2020) using the same wind clustered wind data investigates the impact of mass and aerodynamic efficiency on AWES performance. Adding a design optimization to the `awebox` model enables location-specific aircraft and tether investigation.

7.1 Acknowledgments and funding sources

7.2 Author contribution

Markus Sommerfeld evaluated the data and wrote the manuscript in consultation with and under the supervision of Curran Crawford. Martin Dörenkämper set up the numerical offshore simulation and contributed to the meteorological evaluation of the data and reviewed the manuscript. Jochem De Schutter co-developed the optimization model and helped to write and reviewe this manuscript.

645 References

Abramowitz, M. and Stegun, I. A., eds.: Handbook of Mathematical Functions with Formulas, Graphs and Mathematical Tables, Dover Publications, Inc., New York, 1965.

Airborne Wind Europe: ~~Airborne Wind Energy Glossary,~~ Glossary – definitions of AWE-specific terms https://airbornewindeurope.org/resources/glossary-2/, last accessed: 2022-03-29, 2021.

650 ~~Ampyx:~~ Ampyx Power BV, https://www.ampyxpower.com/, 2020. last accessed: dd-mm-yyyy

Archer, C. L., Colle, B. A., Veron, D. L., Veron, F., and Sienkiewicz, M. J.: On the predominance of unstable atmospheric conditions in the marine boundary layer offshore of the U.S. northeastern coast, Journal of Geophysical Research: Atmospheres, 121, 8869–8885, https://doi.org/10.1002/2016JD024896, 2016.

Argatov, I. and Silvennoinen, R.: Efficiency of Traction Power Conversion Based on Crosswind Motion, in: Airborne Wind Energy, edited 655 by Ahrens, U., Diehl, M., and Schmehl, R., pp. 65–79, Springer, Berlin, Heidelberg, https://doi.org/10.1007/978-3-642-39965-7_4, 2013.

Argatov, I., Rautakorpi, P., and Silvennoinen, R.: Estimation of the mechanical energy output of the kite wind generator, Renewable Energy, 34, 1525–1532, https://doi.org/10.1016/j.renene.2008.11.001, 2009.

Arya, P. and Holton, J.: Introduction to Micrometeorology, International Geophysics, Elsevier Science, 2001.

Aull, M., Stough, A., and Cohen, K.: Design Optimization and Sizing for Fly-Gen Airborne Wind Energy Systems, Automation, 1, 1–16, 660 https://doi.org/10.3390/automation1010001, 2020.

Banta, R. M.: Stable-boundary-layer regimes from the perspective of the low-level jet, Acta Geophysica, 56, 58–87, https://doi.org/10.2478/s11600-007-0049-8, 2008.

Bechtle, P., Schelbergen, M., Schmehl, R., Zillmann, U., and Watson, S.: Airborne wind energy resource analysis, Renewable Energy, 141, 1103 – 1116, ~~https://doi.org/~~ https://doi.org/10.1016/j.renene.2019.03.118, 2019.

665 Bronnenmeyer, T.: Optimal Control for Multi-Kite Emergency Trajectories, Master's thesis, University of Stuttgart, https://cdn.syscop.de/publications/Bronnenmeyer2018.pdf, last accessed: 2022-11-09, 2018.

Carl von Ossietzky Universität Oldenburg: EDDY @ONLINE, https://www.uni-oldenburg.de/fk5/wr/hochleistungsrechnen/hpc-facilities/eddy/, 2018. last accessed: dd-mm-yyyy

Cherubini, A., Papini, A., Vertechy, R., and Fontana, M.: Airborne Wind Energy Systems: A review of the technologies, Renewable and 670 Sustainable Energy Reviews, 51, 1461–1476, https://doi.org/10.1016/j.rser.2015.07.053, 2015.

De Schutter, J., Leuthold, R., Bronnenmeyer, T., Paelinck, R., and Diehl, M.: Optimal control of stacked multi-kite systems for utility-scale airborne wind energy, in: 2019 IEEE 58th Conference on Decision and Control (CDC), pp. 4865–4870, https://doi.org/10.1109/CDC40024.2019.9030026, 2019.

De Schutter, J., Malz, E., Leuthold, R., Bronnenmeyer, T., Paelinck, R., and Diehl, M.: awebox: Modelling and optimal control of single- 675 and multiple-kite systems for airborne wind energy, https://github.com/awebox, last accessed: 2021-10-11, 2020.

Dee, D. P., Uppala, S. M., Simmons, A. J., Berrisford, P., Poli, P., Kobayashi, S., Andrae, U., Balmaseda, M. A., Balsamo, G., Bauer, P., Bechtold, P., Beljaars, A. C. M., van de Berg, L., Bidlot, J., Bormann, N., Delsol, C., Dragani, R., Fuentes, M., Geer, A. J., Haimberger, L., Healy, S. B., Hersbach, H., Hólm, E. V., Isaksen, L., Kållberg, P., Köhler, M., Matricardi, M., McNally, A. P., Monge-Sanz, B. M., Morcrette, J.-J., Park, B.-K., Peubey, C., de Rosnay, P., Tavolato, C., Thépaut, J.-N., and Vitart, F.: The ERA-Interim reanalysis: 680 configuration and performance of the data assimilation system, Quarterly Journal of the Royal Meteorological Society, 137, 553–597, https://doi.org/10.1002/qj.828, 2011.

Diehl, M.: Airborne Wind Energy: Basic Concepts and Physical Foundations, in: Airborne Wind Energy, edited by Ahrens, U., Diehl, M., and Schmehl, R., pp. 3–22, Springer, Berlin Heidelberg https://doi.org/10.1007/978-3-642-39965-7_1, 2013.

Donlon, C. J., Martin, M., Stark, J., Roberts-Jones, J., Fiedler, E., and Wimmer, W.: The Operational Sea Surface Temperature and Sea Ice Analysis (OSTIA) system, Remote Sensing of Environment, 116, 140–158, https://doi.org/10.1016/j.rse.2010.10.017, 2012.

Dörenkämper, M., Optis, M., Monahan, A., and Steinfeld, G.: On the Offshore advection of Boundary-Layer Structures and the Influence on Offshore Wind Conditions, Boundary-Layer Meteorol., 155, 459–482, https://doi.org/10.1007/s10546-015-0008-x, 2015.

Dörenkämper, M., Stoevesandt, B., and Heinemann, D.: Derivation of an offshore wind index for the German bight from high-resolution mesoscale simulation data, Proceedings of DEWEK - German Offshore Wind Energy Conference, p. 5, http://publica.fraunhofer.de/documents/N-484817.html, 2017. last accessed: dd-mm-yyyy

Dörenkämper, M., Olsen, B. T., Witha, B., Hahmann, A. N., Davis, N. N., Barcons, J., Ezber, Y., García-Bustamante, E., González-Rouco, J. F., Navarro, J., Sastre-Marugán, M., Sīle, T., Trei, W., Žagar, M., Badger, J., Gottschall, J., Sanz Rodrigo, J., and Mann, J.: The Making of the New European Wind Atlas – Part 2: Production and Evaluation, Geosci. Model Dev. Discuss., 2020, 1–37, https://doi.org/10.5194/gmd-2020-23, 2020.

Echeverri, P., Fricke, T., Homsy, G., and Tucker, N.: The Energy Kite - Selected Results From the Design, Development and Testing of Makani's Airborne Wind Turbines - Part 1, Technical Report, Makani Power, https://storage.googleapis.com/x-prod.appspot.com/files/Makani_TheEnergyKiteReport_Part1.pdf, last accessed: 2022-11-09, 2020.

Eijkelhof, D., Rapp, S., Fasel, U., Gaunaa, M., and Schmehl, R.: Reference Design and Simulation Framework of a Multi-Megawatt Airborne Wind Energy System, Journal of Physics: Conference Series, 1618, https://doi.org/10.1088/1742-6596/1618/3/032020, 2020.

Ellis, G. and Ferraro, G.: The Social Acceptance of Wind Energy: Where we stand and the path ahead., EUR - Scientific and Technical Research Reports, European Commission, https://doi.org/10.2789/696070, 2016.

Emeis, S.: Wind energy meteorology : atmospheric physics for wind power generation, Green Energy and Technology, Springer, Berlin Heidelberg, https://doi.org/10.1007/978-3-642-30523-8, 12.02.03; LK 01, 2013.

Faggiani, P. and Schmehl, R.: Design and Economics of a Pumping Kite Wind Park, in: Airborne Wind Energy: Advances in Technology Development and Research, edited by Schmehl, R., pp. 391–411, Springer Singapore, Singapore, https://doi.org/10.1007/978-981-10-1947-0_16, 2018.

Fagiano, L. and Milanese, M.: Airborne Wind Energy: An overview, in: 2012 American Control Conference (ACC), pp. 3132–3143, IEEE, https://doi.org/10.1109/ACC.2012.6314801, 2012.

Floors, R., Batchvarova, E., Gryning, S.-E., Hahmann, A. N., Peña, A., and Mikkelsen, T.: Atmospheric boundary layer wind profile at a flat coastal site - wind speed lidar measurements and mesoscale modeling results, Advances in Science and Research, 6, 155–159, https://doi.org/10.5194/asr-6-155-2011, 2011.

Gaertner, E., Rinker, J., Sethuraman, L., Zahle, F., Anderson, B., Barter, G. E., Abbas, N. J., Meng, F., Bortolotti, P., Skrzypinski, W., Scott, G. N., Feil, R., Bredmose, H., Dykes, K., Shields, M., Allen, C., and Viselli, A.: IEA Wind TCP Task 37: Definition of the IEA 15-Megawatt Offshore Reference Wind Turbine, Tech. rep., NREL, https://doi.org/10.2172/1603478, 2020.

Gros, S., Zanon, M., and Diehl, M.: A relaxation strategy for the optimization of airborne wind energy systems, in: Control Conference (ECC), 2013 European, pp. 1011–1016, IEEE, Zurich, Switzerland, https://doi.org/10.23919/ECC.2013.6669670, 2013.

Haas, T., Schutter, J. D., Diehl, M., and Meyers, J.: Wake characteristics of pumping mode airborne wind energy systems, Journal of Physics: Conference Series, 1256, 012 016, https://doi.org/10.1088/1742-6596/1256/1/012016, 2019.

Hahmann, A. N., Sile, T., Witha, B., Davis, N. N., Dörenkämper, M., Ezber, Y., García-Bustamante, E., González Rouco, J. F., Navarro, J., Olsen, B. T., and Söderberg, S.: The Making of the New European Wind Atlas, Part 1: Model Sensitivity, Geosci. Model Dev. Discuss., 2020, 1–33, https://doi.org/10.5194/gmd-2019-349, 2020.

Heilmann, J. and Houle, C.: Economics of Pumping Kite Generators, in: Airborne Wind Energy, edited by Ahrens, U., Diehl, M., and Schmehl, R., pp. 271–284, Springer Berlin Heidelberg, ~~Berlin, Heidelberg,~~ https://doi.org/10.1007/978-3-642-39965-7_15, 2013.

Hersbach, H. and Dick, D.: ERA5 reanalysis is in production, http://www.ecmwf.int/en/newsletter/147/news/era5-reanalysis-production, last accessed: 2019-10-22, 2016.

Houska, B. and Diehl, M.: Optimal control for power generating kites, in: 2007 European Control Conference (ECC), pp. 3560–3567, IEEE, https://doi.org/10.23919/ECC.2007.7068861, 2007.

HSL: HSL. A collection of Fortran codes for large scale scientific computation, http://www.hsl.rl.ac.uk/, last accessed: 2022-03-14, 2020.

Jonkman, J., Butterfield, S., Musial, W., and Scott, G.: Definition of a 5-MW Reference Wind Turbine for Offshore System Development, Tech. rep., NREL, https://doi.org/10.2172/947422, 2009.

Kruijff, M. and Ruiterkamp, R.: A Roadmap Towards Airborne Wind Energy in the Utility Sector, in: Airborne Wind Energy: Advances in Technology Development and Research, edited by Schmehl, R., pp. 643–662, Springer Singapore, ~~Singapore,~~ https://doi.org/10.1007/978-981-10-1947-0_26, 2018.

Leuthold, R., De Schutter, J., Malz, E., Licitra, G., Gros, S., and Diehl, M.: Operational Regions of a Multi-Kite AWE System, in: 2018 European Control Conference (ECC), pp. 52–57, Limassol, Cyprus, https://doi.org/10.23919/ECC.2018.8550199, 2018.

Licitra, G.: Identification and optimization of an airborne wind energy system, Ph.D. thesis, University of Freiburg, https://doi.org/10.6094/UNIFR/16226, 2018.

Licitra, G., Koenemann, J., Bürger, A., Williams, P., Ruiterkamp, R., and Diehl, M.: Performance assessment of a rigid wing Airborne Wind Energy pumping system, Energy, 173, 569–585, https://doi.org/10.1016/j.energy.2019.02.064, 2019.

Loyd, M. L.: Crosswind kite power (for large-scale wind power production), Journal of Energy, 4, 106–111, https://doi.org/10.2514/3.48021, 1980.

Lunney, E., Ban, M., Duic, N., and Foley, A.: A state-of-the-art review and feasibility analysis of high altitude wind power in Northern Ireland, Renewable and Sustainable Energy Reviews, 68, 899 – 911, ~~https://doi.org/~~https://doi.org/10.1016/j.rser.2016.08.014, 2017.

Malz, E., Koenemann, J., Sieberling, S., and Gros, S.: A reference model for airborne wind energy systems for optimization and control, Renewable Energy, 140, 1004 – 1011, https://doi.org/10.1016/j.renene.2019.03.111, 2019.

Malz, E., Hedenus, F., Göransson, L., Verendel, V., and Gros, S.: Drag-mode airborne wind energy vs. wind turbines: An analysis of power production, variability and geography, Energy, 193, 116765, ~~https://doi.org/~~https://doi.org/10.1016/j.energy.2019.116765, 2020a.

Malz, E., Verendel, V., and Gros, S.: Computing the power profiles for an Airborne Wind Energy system based on large-scale wind data, Renewable Energy, 162, 766 – 778, ~~https://doi.org/~~https://doi.org/10.1016/j.renene.2020.06.056, 2020b.

Molina-García, A., Fernández-Guillamón, A., Gómez-Lázaro, E., Honrubia-Escribano, A., and Bueso, M. C.: Vertical Wind Profile Characterization and Identification of Patterns Based on a Shape Clustering Algorithm, IEEE Access, 7, 30890–30904, https://doi.org/10.1109/ACCESS.2019.2902242, 2019.

Nakanishi, M. and Niino, H.: Development of an Improved Turbulence Closure Model for the Atmospheric Boundary Layer, Journal of the Meteorological Society of Japan, 87, 895–912, https://doi.org/10.2151/jmsj.87.895, 2009.

Obukhov, A. M.: Turbulence in an atmosphere with a non-uniform temperature, Boundary-Layer Meteorology, 2, 7–29, https://doi.org/10.1007/BF00718085, 1971.

offshorewind.biz: Ampyx Power Taking First Steps Towards MW-Scale Kite, Online, https://www.offshorewind.biz/2018/12/04/ampyx-power-taking-first-steps-towards-mw-scale-kite/, last accessed: 2022-03-14, 2018.

Olauson, J.: ERA5: The new champion of wind power modelling?, Renewable Energy, 126, 322–331, https://doi.org/10.1016/j.renene.2018.03.056, 2018.

Optis, M., Monahan, A., and Bosveld, F. C.: Limitations and breakdown of Monin–Obukhov similarity theory for wind profile extrapolation under stable stratification, Wind Energy, 19, 1053–1072, https://doi.org/10.1002/we.1883, 2016.

Peña, A., Gryning, S.-E., and Floors, R.: Lidar observations of marine boundary-layer winds and heights: a preliminary study, Meteorologische Zeitschrift, 24, 581–589, https://doi.org/10.1127/metz/2015/0636, 2015.

Pedregosa, F., Varoquaux, G., Gramfort, A., Michel, V., Thirion, B., Grisel, O., Blondel, M., Prettenhofer, P., Weiss, R., Dubourg, V., Vanderplas, J., Passos, A., Cournapeau, D., Brucher, M., Perrot, M., and Duchesnay, E.: Scikit-learn: Machine Learning in Python, Journal of Machine Learning Research, 12, 2825–2830, https://doi.org/10.48550/arXiv.1201.0490, 2011.

Ranneberg, M., Wölfle, D., Bormann, A., Rohde, P., Breipohl, F., and Bastigkeit, I.: Fast Power Curve and Yield Estimation of Pumping Airborne Wind Energy Systems, in: Airborne Wind Energy: Advances in Technology Development and Research, edited by Schmehl, R., pp. 623–641, Springer Singapore, Singapore, https://doi.org/10.1007/978-981-10-1947-0_25, 2018.

Salvação, N. and Guedes Soares, C.: Wind resource assessment offshore the Atlantic Iberian coast with the WRF model, Energy, 145, 276 – 287, https://doi.org/https://doi.org/10.1016/j.energy.2017.12.101, 2018.

Schelbergen, M., Kalverla, P. C., Schmehl, R., and Watson, S. J.: Clustering wind profile shapes to estimate airborne wind energy production, Wind Energy Science, 5, 1097–1120, https://doi.org/10.5194/wes-5-1097-2020, 2020.

Schmehl, R., Noom, M., and van der Vlugt, R.: Traction Power Generation with Tethered Wings, in: Airborne Wind Energy, edited by Ahrens, U., Diehl, M., and Schmehl, R., chap. 2, pp. 23–45, Springer, Berlin, Heidelberg, https://doi.org/10.1007/978-3-642-39965-7_2, 2013.

Sempreviva, A. M. and Gryning, S.-E.: Humidity fluctuations in the marine boundary layer measured at a coastal site with an infrared humidity sensor, Boundary-Layer Meteorology, 77, 331–352, https://doi.org/10.1007/BF00123531, 1996.

Skamarock, W., Klemp, J., Dudhia, J., Gill, D., Barker, D., Duda, M., Huang, X., Wang, W., and Powers, J.: A description of the advanced research WRF version 3, Tech. Rep. NCAR/TN–475+STR, NCAR - National Center for Atmospheric Research, Boulder, Colorado, USA, https://doi.org/10.5065/D68S4MVH, 2008.

Skamarock, W. C., Klemp, J. B., Dudhia, J., and Gill, D. O.: A Description of the Advanced Research WRF Model Version 4.3, Technical Report, UCAR, https://doi.org/10.5065/1dfh-6p97, 2021.

Sommerfeld, M., Crawford, C., Monahan, A., and Bastigkeit, I.: LiDAR-based characterization of mid-altitude wind conditions for airborne wind energy systems, Wind Energy, 22, 1101–1120, https://doi.org/https://doi.org/10.1002/we.2343, 2019a.

Sommerfeld, M., Dörenkämper, M., Steinfeld, G., and Crawford, C.: Improving mesoscale wind speed forecasts using lidar-based observation nudging for airborne wind energy systems, Wind Energy Science, 4, 563–580, https://doi.org/10.5194/wes-4-563-2019, 2019b.

Sommerfeld, M., Dörenkämper, M., De Schutter, J., and Crawford, C.: Ground-generation airborne wind energy design space exploration, Wind Energy Science Discussions, 2020, 1–34, https://doi.org/10.5194/wes-2020-123, 2020.

Stull, R.: An Introduction to Boundary Layer Meteorology, Atmospheric and Oceanographic Sciences Library, Springer Netherlands, https://doi.org/10.1007/978-94-009-3027-8, 1988.

van der Vlugt, R., Bley, A., Noom, M., and Schmehl, R.: Quasi-steady model of a pumping kite power system, Renewable Energy, 131, 83 – 99, https://doi.org/10.1016/j.renene.2018.07.023, 2019.

Waechter, A. and Laird, C.: Ipopt (Interior Point OPTimizer), https://github.com/coin-or/Ipopt, last accessed: 2022-03-14, 2016.

795 Witha, B., Hahmann, A., Sīle, T., Dörenkämper, M., Ezber, Y., García-Bustamante, E., González-Rouco, J. F., Leroy, G., and Navarro, J.: WRF model sensitivity studies and specifications for the NEWA mesoscale wind atlas production runs, Technical report, 73 pages, ~~The NEWA consortium,~~ : Deliverable D4.3 2019. https://doi.org/10.5281/zenodo.2682604
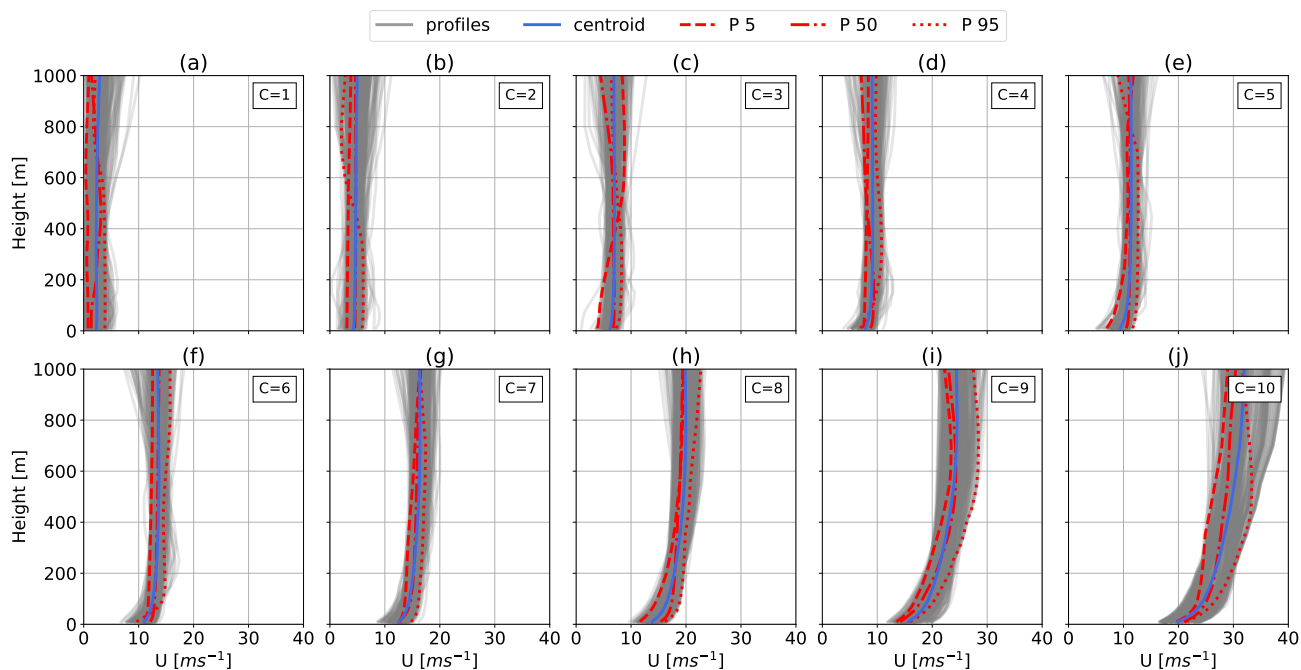
Figure A1. Vertical offshore wind speed profiles categorized into $k = 10$ clustered using the k-means clustering algorithm. Later analyses use $k = 20$ clusters. The average profile (centroid) is shown in blue and the profiles associated with this cluster are shown in gray. Clusters 1 to 10 (a-j) are sorted and labeled in ascending order of average centroid wind speed between 100 m and 400 m. The corresponding cluster frequency f for each cluster C is shown in Figure 5. The red lines mark the wind speed profile with the 5th, 50th and 95th percentile of average wind between 100 and 400 m within each cluster.
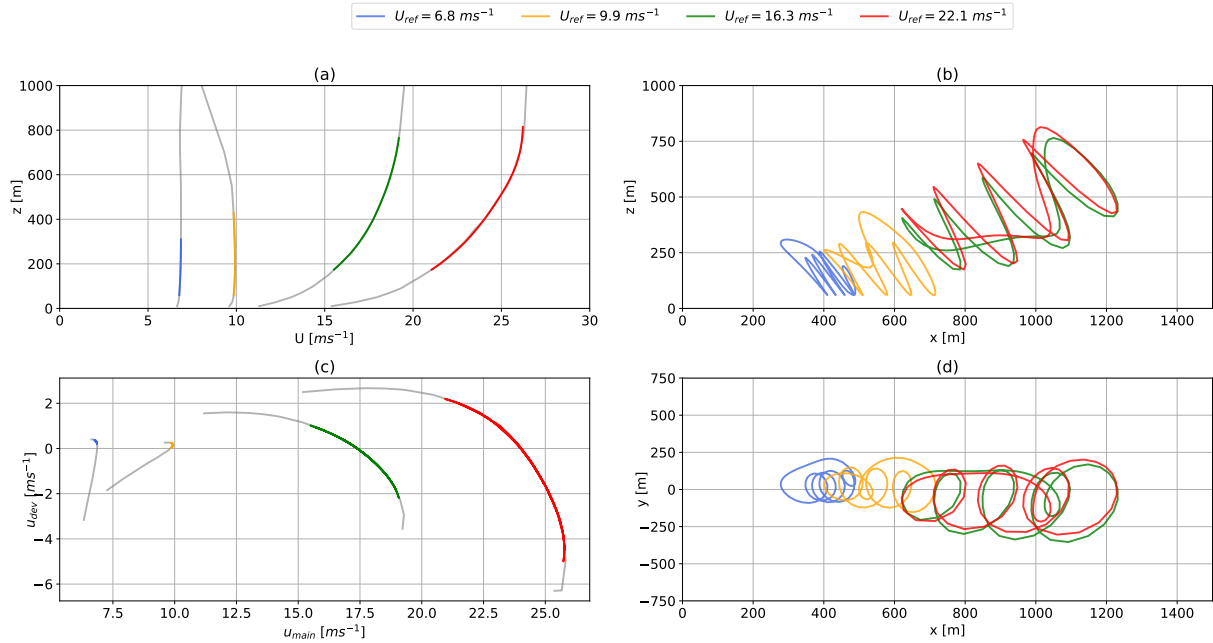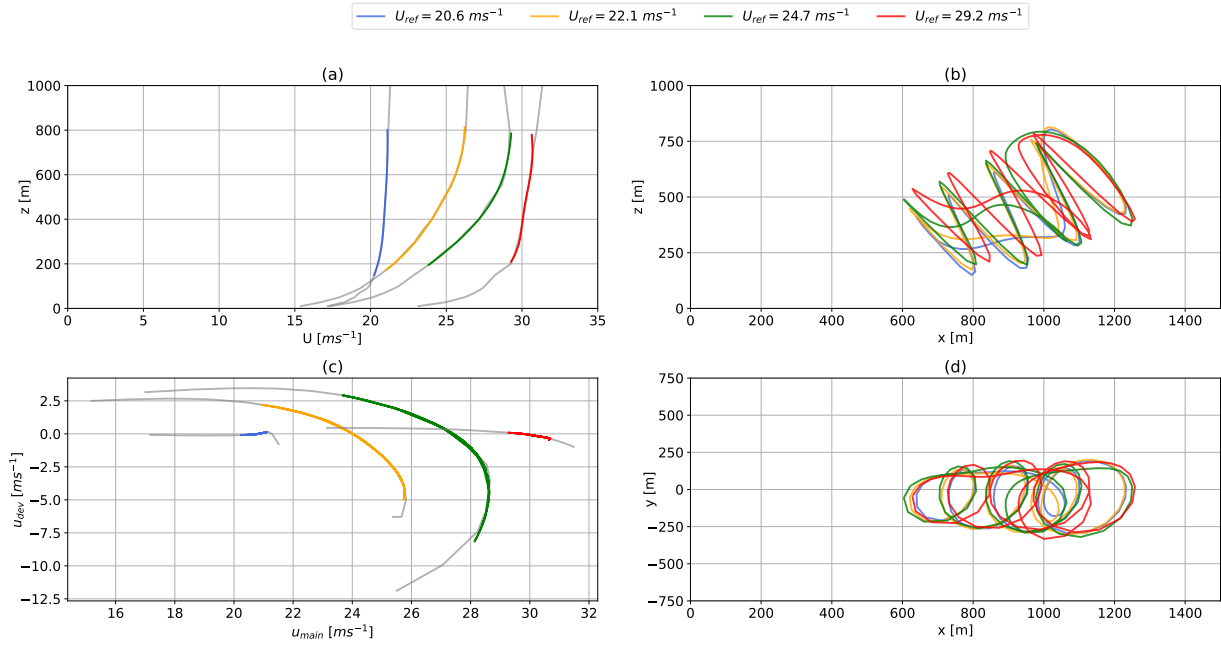
Figure A2. Exemplary offshore trajectories. Wind data are based on sampled WRF-simulated clusters (Section 2). Wind speed magnitude (a), and hodograph (top view) of wind velocity up to 1000 m (c). The highlighted sections indicate operating wind conditions. Panel (b) and panel (d) shows the side and top view of the corresponding awebox-optimized trajectories. The reference wind speed in the legend is $U_{\mathrm{ref}} = \overline{U}(100 \text{ m} \leq z_{\mathrm{ref}} \leq 400 \text{ m})$. The results correspond to the time series shown in Figure A3.
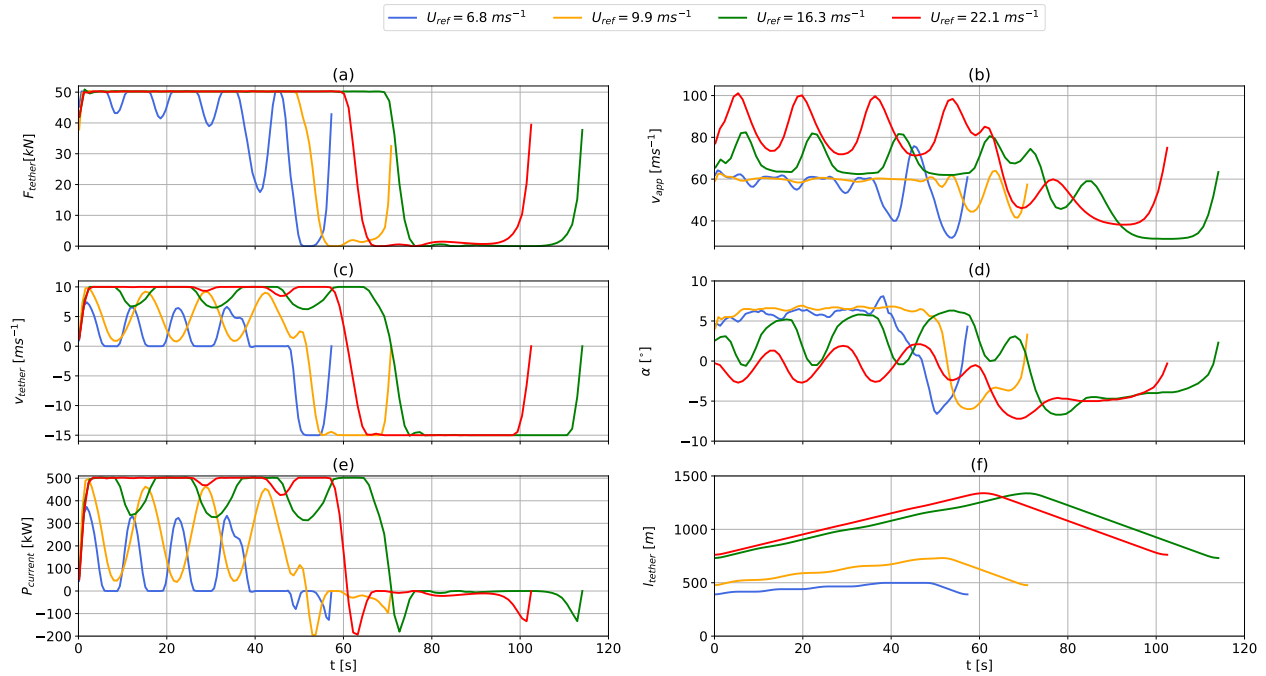
Figure A3. Time series of instantaneous tether tension (a), apparent wind speed (b), tether-reeling speed (c), angle of attack α (d), power (e) and tether length (f). The results correspond to the trajectories, based on sampled offshore WRF-simulated wind data, shown in Figure 12.

Figure A4. Exemplary offshore high wind speed trajectories. Wind data are based on sampled WRF-simulated clusters (Section 2). Wind speed magnitude (a), and hodograph (top view) of wind velocity up to 1000 m (c). The highlighted sections indicate operating wind conditions. Panel (b) and panel (d) shows the side and top view of the corresponding awebox-optimized trajectories. The reference wind speed in the legend is $U_{\mathrm{ref}} = \overline{U}(100 \text{ m} \leq z_{\mathrm{ref}} \leq 400 \text{ m})$. The results correspond to the time series shown in Figure 16.